Petroleum Science 23 (2026) 5474–5496

Contents lists available at ScienceDirect

Petroleum Science

journal homepage: www.keaipublishing.com/en/journals/petroleum-science

Original Paper

Stress and frequency dependence of wave reflection and transmission in patchy-saturated porous media

Jia-Yun Li [a], Zhao-Yun Zong [a,*], Xing-Yao Yin [a], Zhi-Wei Miao [b], Shi-Kai Li [b], Wei Xiao [b]

[a] State Key Laboratory of Deep Oil and Gas, China University of Petroleum (East China), Qingdao, 266580, Shandong, China
[b] Sinopec Exploration Company, Chengdu, 610041, Sichuan, China

ARTICLE INFO

Article history:
Received 1 December 2025
Received in revised form
14 February 2026
Accepted 19 April 2026
Available online 22 April 2026

Edited by Meng-Jiao Zhou

Keywords:
Wave-induced fluid flow (WIFF)
Poro-acoustoelasticity (PAE) theory
Effective stress
Wave reflection and transmission
Patchy-saturated porous media

ABSTRACT

Partially saturated porous media are frequently encountered in the subsurface. However, the wave reflection and transmission (R/T) characteristics of such media under in situ stress are not fully understood. To address this issue, we derive an exact R/T coefficient equation for an inhomogeneous plane wave incident obliquely at the interface between two dissimilar stressed patchy-saturated porous media, based on our new stress- and frequency-dependent rock physics model. The new model simultaneously incorporates the wave-induced fluid flow (WIFF) mechanisms at macroscopic, mesoscopic, and microscopic scales. Specifically, the nonlinear deformation of cracks is incorporated into the microscopic squirt-flow and mesoscopic patchy-saturated models to modify the solid frame and fluid moduli, while the poro-acoustoelasticity (PAE) theory is incorporated to account for macroscopic global flow and in situ stress effects. The modeling results indicate that P- and S-wave dispersion and attenuation decrease with increasing effective stress, but increase with rising water saturation. The opposite effects can be attributed to the closure of compliant cracks and the increased viscosity of the pore fluid, respectively. By comparing our model with published models and experimental data, we confirm its validity and reliability. Subsequently, the variations of the R/T coefficients with incident angle, effective stress, frequency, inhomogeneity angle, and water saturation are further analyzed. The findings demonstrate that the R/T coefficients exhibit significant dependence on effective stress and water saturation across the entire range of incidence angles, whereas the effect of inhomogeneity angle occurs primarily near the critical angle. With increasing effective stress, the critical angle grows, and at small incidence angles, fast P-wave reflection decreases while transmission increases, these effects diminishing at higher stress. The energy conservation at the interface further illustrates the validity of our R/T coefficient equation.

1. Introduction

The subsurface medium often exhibits complex pore structures and the coexistence of multiphase fluids due to the combined effects of in situ stress and structural movements (Ba et al., 2023, 2024; Fagbemi et al., 2018, 2020; Kumar et al., 2018). Understanding the characteristics of elastic wave dispersion and attenuation in partially saturated porous media under in situ stress, along with their reflection and transmission (R/T) properties at the interface, is of great significance to research in hydrogeology, engineering geology, petroleum engineering, seismology, and hydrocarbon exploration (Chen et al., 2023a, 2024a; Jiang et al., 2025; Wang et al., 2020; Yang and Fu, 2025).

The propagation of elastic waves through partially saturated porous media induces fluid flow at different scales, leading to velocity dispersion and attenuation. To quantitatively describe this phenomenon, the theory of wave-induced fluid flow (WIFF) has been proposed. Based on the spatial scale of fluid flow relative to the wavelength and pore size, WIFF can be categorized into three scales: macroscopic, mesoscopic, and microscopic. Biot (1956, 1962) first proposed poroelasticity theory, which characterizes the dissipation of wave energy resulting from the macroscopic flow of pore fluid relative to the solid skeleton in an isotropic fluid-saturated porous medium, and subsequently predicted the existence of a slow P-wave. However, this theory cannot account for

* Corresponding author.
E-mail address: zongzhaoyun@upc.edu.cn (Z.-Y. Zong).
Peer review under the responsibility of China University of Petroleum (Beijing).

https://doi.org/10.1016/j.petsci.2026.04.032
1995-8226/

the velocity dispersion and attenuation observed in the low-frequency range, which are widely attributed to mesoscopic WIFF resulting from the heterogeneous distribution of the solid skeleton or pore fluid (Ba et al., 2017; He et al., 2024b; Pride et al., 2004; Sun et al., 2016; Zhang and He, 2015; Zheng et al., 2017). To quantitatively explain the loss mechanism caused by partially saturated fluid, White (1975) assumed a concentric-sphere fluid distribution and proposed the patchy saturation model. However, due to the approximate theory used in the model, the predicted velocities in the low-frequency limit do not agree well with the Gassmann-Wood predictions. Therefore, Dutta and Odé (1979a, 1979b) and Dutta and Seriff (1979) introduced the necessary corrections. Subsequently, a series of theoretical and experimental studies on patchy saturation are conducted (Johnson, 2001; Mews and Lozovyi, 2025; Sun et al., 2022), effectively explaining the wave dispersion and attenuation observed in the seismic frequency range. In addition, when waves propagate through rocks with complex pore structures, the energy dissipation caused by microscopic squirt flow between compliant pores (cracks) and stiff pores cannot be neglected (Alkhimenkov and Quintal, 2024; Chen et al., 2025; Gurevich et al., 2010). Considering the WIFF mechanisms at three scales, Shi et al. (2024) developed a multiscale model that provides a theoretical basis for interpreting wave dispersion and attenuation characteristics of partially saturated porous media over a broad frequency band. WIFF theory is also used to characterize the R/T behavior of fluid-saturated porous media. Based on Biot poroelasticity theory, a series of studies on plane wave R/T have been carried out. Early research focused on the case of normal incidence (Geertsma and Smit, 1961; Stoll, 1977). Dutta and Odé (1983) further extended the research to the more general case of oblique incidence. Based on this, the R/T characteristics of waves at the fluid/porous solid interface (Denneman et al., 2002; Sharma, 2004; Wu et al., 1990), and at the interface between two porous homogeneous media (Gurevich et al., 2004; Qi et al., 2021; Zhao et al., 2015) are further analyzed as functions of incident angle and frequency. Considering that mesoscale WIFF in heterogeneous rocks can lead to wave velocity dispersion and attenuation at seismic frequencies, significantly influencing wave R/T behavior, the Rayleigh's spherical bubble oscillation model is incorporated into the conventional Biot poroelasticity theory (Kumari et al., 2025; Wang et al., 2020). At the same time, an inhomogeneity angle (the angle between the propagation direction and the direction of maximum attenuation) is introduced into the displacement potential (Hou et al., 2022, 2023; Kumari et al., 2017; Sharma, 2013). Although in-situ stress is ubiquitous in the subsurface, its influence has not been incorporated in the aforementioned R/T studies.

Poro-acoustoelasticity (PAE) theory, as a generalization of poroelasticity and acoustoelasticity, provides a theoretical basis for characterizing the effect of in-situ stress on wave velocity dispersion and attenuation in fluid-saturated porous media. Taking into account the finite deformation of solid under in situ stress, acoustoelasticity theory was developed as an extension of classic elasticity (Biot, 1972, 1973; Chen et al., 2024b; Pao, 1984; Sripanich et al., 2021; Thurston and Brugger, 1964). It retains the cubic terms in the strain energy function, in addition to the conventional quadratic terms, and introduces third-order elastic constants (3oECs) to describe the stress-dependent behavior of solid media. However, Winkler and McGowan (2004) demonstrated that the classic 3oEC theory does not fully capture the stress-dependent velocity behavior in water-saturated rocks, based on a comparison between theoretical predictions from acoustoelasticity theory and experimental observations in both dry and saturated conditions. To address this issue, the poro-acoustoelasticity (PAE) theory was developed, which accounts for the finite deformations of both the solid matrix and the pore fluid, thereby extending the applicability of the acoustoelasticity theory to fluid-saturated media (Ba et al., 2013; Liu et al., 2021). However, this theory only considers the linear effect of stress on static strain and therefore it cannot explain the exponential variation of elastic wave velocity observed in experiments. Consequently, Fu and Fu (2018), based on the dual-porosity model (Shapiro, 2003), while Ling et al. (2021), based on the pore structure model (David and Zimmerman, 2012), incorporated the nonlinear stress dependence of cracks into PAE theory, thereby extending its applicability to a broad stress range. Recently, based on the PAE theory, Chen et al. (2024a) incorporated in-situ stress into the analysis of plane wave R/T characteristics and proposed general boundary conditions, demonstrating the stress dependence of the R/T coefficients. However, to the best of our knowledge, existing PAE theories have not yet considered the effects of micro- and meso-scale WIFF, potentially leading to a misleading understanding of the stress- and frequency-dependent wave R/T behaviors in partially saturated porous media.

In this study, a stress- and frequency-dependent rock physics model is proposed to analyze the plane wave R/T characteristics at the interface of patchy-saturated porous media containing wedge-shaped cracks (see Fig. 1). Firstly, the modified frame and fluid moduli are derived using the squirt-flow model (Chen et al., 2025) and the patchy-saturated model (White, 1975; Carcione et al., 2003) corrected by Dutta and Seriff (1979), wherein the dual-porosity model is employed to incorporate the influence of effective stress on the nonlinear deformation of stiff pores and cracks. Then, the modified moduli are incorporated into the PAE model (Chen et al., 2024a), yielding a dynamic equation that simultaneously accounts for energy dissipation at the macro-, meso-, and micro-scale under effective stress. Based on our new model, we analyze the variations in the dispersion and attenuation of fast and slow P-waves as well as S-wave with respect to effective stress, frequency, water saturation, and crack aspect ratio. Comparison with previously published experimental data confirm the validity of our proposed model. Finally, an exact expression for the R/T coefficients of an inhomogeneous plane wave obliquely incident on the interface between two patchy-saturated porous media under effective stress is derived. The reliability of the coefficients is verified by the principle of energy conservation. Furthermore, we systematically analyze the effects of effective stress, frequency, water saturation, incident angle, and inhomogeneity angle on the R/T coefficients.

2. Theory

2.1. Modified moduli of patchy-saturated porous media under effective stress

When the formation is subjected to in-situ stress, the effective stress acting on the rock skeleton leads to a reduction in porosity, given by (Detournay and Cheng, 1993; Zimmerman et al., 1986)

$$\frac{d\phi}{dp}=\frac{1}{K_{gr}}-(1-\phi)\frac{1}{K_{dr}} \tag{1}$$

where ϕ is porosity, $p=p_c-p_p$ refers to the effective stress (i.e. confining pressure minus pore pressure), K_{gr} and K_{dr} represent the bulk modulus of grain and dry rock skeleton, respectively.

Considering that differences in pore shape (pore aspect ratio) affect pore compressibility, Shapiro (2003) proposed a dual-porosity model that divides rock porosity ϕ into two parts: compliant porosity (cracks) ϕ_c and stiff porosity $[\phi_{s0}+\phi_s']$. Here, ϕ_{s0} refers to the stiff porosity under zero effective stress, and ϕ_s' represents the variation in stiff porosity caused by effective stress,

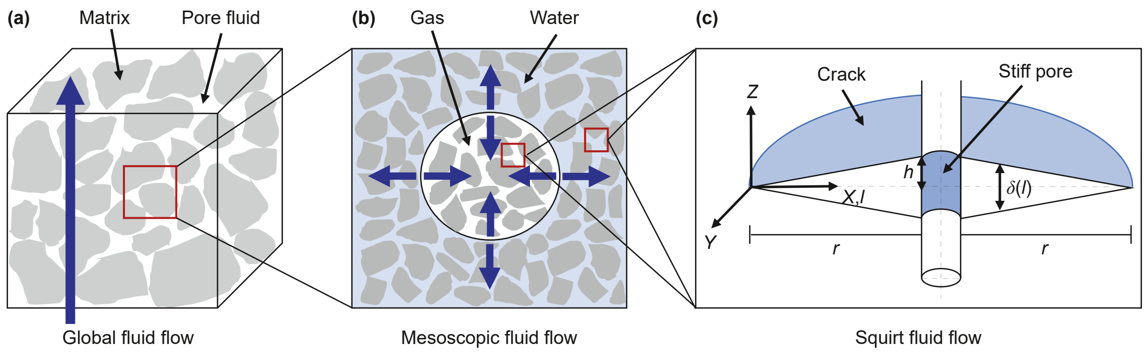

Fig. 1. Schematic diagram of **(a)** global fluid flow, **(b)** mesoscopic fluid flow and **(c)** squirt fluid flow in patchy-saturated porous media containing wedge-shaped cracks.

with $\phi_{s0} \gg |\phi_s'| \gg \phi_c$. In porous sandstones, the typical orders of magnitude are ϕ_{s0} ~10^{-1}, $|\phi_s'|$ ~10^{-2} and ϕ_c ~10^{-3}.

To simplify the equation, a Taylor expansion is applied to the bulk compressibility of dry rock $1/K_{dr}$, and higher-order terms are neglected, written as

$$\frac{1}{K_{dr}}(\phi_{s0}+\phi_s',\phi_c)=\frac{1}{K_{drs}}\left[1+\theta_s\phi_s'+\theta_c\phi_c\right] \tag{2}$$

where K_{drs} represents the bulk modulus of the dry rock with closed compliant cracks. The stress sensitivity coefficients (SSC) of bulk modulus are

$$\theta_s=-\frac{1}{K_{drs}}\frac{\partial K_{dr}}{\partial \phi_s'},\theta_c=-\frac{1}{K_{drs}}\frac{\partial K_{dr}}{\partial \phi_c} \tag{3}$$

Since θ_s is of order 1, while θ_c is on the order of or larger than 10^2 (Shapiro, 2003). Combining the relationships $\theta_s\phi_s' \ll \theta_c\phi_c$ and $d\phi = d\phi_s' + d\phi_c$, then substituting Eq. (2) into Eq. (1), yields

$$\begin{aligned}d\phi_s'+d\phi_c=\Big[K_{gr}^{-1}-\Big(&1+\theta_c\phi_c-\phi_c-\theta_c\phi_c^2-\phi_{s0}-\theta_c\phi_c\phi_{s0}\\&-\phi_s'-\theta_c\phi_c\phi_s'\Big)K_{drs}^{-1}\Big]dp\end{aligned} \tag{4}$$

If all cracks are closed, i.e., $\phi_c = 0$, the expression for the variation of stiff porosity with effective stress is obtained as

$$\frac{d\phi_s'}{dp}=K_{gr}^{-1}-(1-\phi_{s0}-\phi_s')K_{drs}^{-1} \tag{5}$$

Then, the variation of cracks can be expressed as

$$\frac{d\phi_c}{dp}=\left(\theta_c\phi_c\phi_{s0}+\theta_c\phi_c\phi_s'+\theta_c\phi_c^2-\theta_c\phi_c+\phi_c\right)K_{drs}^{-1} \tag{6}$$

Solving the differential Eqs. (5) and (6), and neglecting the negligible value $\theta_c\phi_c^2$, the functions of stiff and compliant porosity under effective stress are yielded as

$$\phi_s'(p)=1-\phi_{s0}-\frac{K_{drs}}{K_{gr}}+\left(\frac{K_{drs}}{K_{gr}}+\phi_{s0}-1\right)\exp\left(\frac{p}{K_{drs}}\right) \tag{7}$$

$$\phi_c(p)=\phi_{c0}\exp\left(\frac{\theta_c\phi_{s0}+\theta_c\phi_s'-\theta_c+1}{K_{drs}}p\right) \tag{8}$$

Then, by substituting Eqs. (7) and (8) into Eq. (2), and based on the assumption that the deformation of cracks has a more significant effect on the rock properties than that of stiff pores (Shapiro, 2003; Chen et al., 2024a), the bulk modulus of dry rock as a function of effective stress is obtained as follows:

$$\frac{1}{K_{dr}(p)}=\frac{1}{K_{drs}}\left[1+\theta_c\phi_{c0}\exp\left(\frac{\theta_c\phi_{s0}+\theta_c\phi_s'-\theta_c+1}{K_{drs}}p\right)\right] \tag{9}$$

Similar to the bulk modulus, the shear modulus can be expressed as

$$\frac{1}{\mu_{dr}(p)}=\frac{1}{\mu_{drs}}\left[1+\theta_{c\mu}\phi_{c0}\exp\left(\frac{\theta_c\phi_{s0}+\theta_c\phi_s'-\theta_c+1}{K_{drs}}p\right)\right] \tag{10}$$

where $\theta_{c\mu} = -\frac{1}{\mu_{drs}}\frac{\partial \mu_{dr}}{\partial \phi_c}$. μ_{drs} is the shear modulus of dry rock without cracks.

Wave propagation through a fluid-saturated porous medium induces fluid pressure gradients between stiff pores and compliant cracks at the microscale, leading to fluid flow. To describe this phenomenon, Chen et al. (2025) developed a squirt-flow model, in which wedge-shaped crack connects to the central stiff pore. By substituting the stress-dependent crack porosity, bulk modulus and shear modulus given in Eqs. (8)–(10) into the formulation, the bulk and shear moduli of the modified frame under effective stress and squirt flow can be yielded as

$$\frac{1}{K_{mf}^{(j)}(p,\omega)}=\frac{1}{K_{drs}}+\frac{1}{\frac{1}{1/K_{dr}(p)-1/K_{drs}}+\frac{1}{\left(1\Big/K_f^{(j)*}-1\Big/K_{gr}\right)\phi_c(p)}},j=1,2 \tag{11}$$

$$\frac{1}{\mu_{mf}^{(j)}(p,\omega)}=\frac{1}{\mu_{dr}(p)}-\frac{4}{15}\left[\frac{1}{K_{dr}(p)}-\frac{1}{K_{mf}^{(j)}(p,\omega)}\right],j=1,2 \tag{12}$$

with

$$K_f^{(j)*}=\left(1-\frac{2}{\sqrt{1-k^2}}+\frac{2}{1+\sqrt{1-k^2}}\right)K_f^{(j)} \tag{13}$$

$$k=\frac{1}{\beta}\sqrt{-\frac{12i\omega\eta^{(j)}}{K_f^{(j)}}} \tag{14}$$

where $\beta = 2h/(2r)$ refers to the crack aspect ratio, $2h$ and $2r$ are the height and length of the cracks, respectively (see Fig. 1(c)). $K_f^{(j)}, j = 1,2$ represent the bulk modulus of gas and water. i represents the imaginary unit. ω represents the angular frequency. $\eta^{(j)}$ refers to the fluid viscosity.

Considering that multiphase fluid mixtures (e.g., water and gas) are commonly present in real formations, wave propagation through patchy-saturated porous media can induce fluid flow between different fluid phases. Based on the patchy-saturated mesoscopic WIFF model (White, 1975; Carcione et al., 2003), and treating $K_{\mathrm{mf}}^{(j)}(p,\omega)$ and $\mu_{\mathrm{mf}}^{(j)}(p,\omega)$ as the bulk and shear moduli of the dry rock, the stress- and frequency-dependent fluid bulk modulus can be expressed as follows:

$$K_{\mathrm{f}}^{\#}(p,\omega)=\frac{\phi(p)\left[K_{\mathrm{sat}}(p,\omega)-K_{\mathrm{mf}}(p,\omega)\right]}{\left(1-\frac{K_{\mathrm{mf}}(p,\omega)}{K_{\mathrm{gr}}}\right)^{2}-\left[K_{\mathrm{sat}}(p,\omega)-K_{\mathrm{mf}}(p,\omega)\right]\left(\frac{1-\phi(p)}{K_{\mathrm{gr}}}-\frac{K_{\mathrm{mf}}(p,\omega)}{K_{\mathrm{gr}}^{2}}\right)} \tag{15}$$

where $\phi(p)=\phi_{\mathrm{s0}}+\phi_{\mathrm{s}}'(p)+\phi_{\mathrm{c}}(p)$ represents the total porosity of the rock. The effective bulk modulus of modified frame can be calculated using equation $K_{\mathrm{mf}}(p,\omega)=1/\left[S_1/K_{\mathrm{mf}}^{(1)}(p,\omega)+S_2/K_{\mathrm{mf}}^{(2)}(p,\omega)\right]$. S_1 and S_2 denote the saturations of gas and water, respectively. The detailed derivation is provided in Appendix A.

2.2. Poro-acoustoelasticity theory incorporating coupled modified moduli

For isotropic fluid-solid two-phase media, the strain potential energy can be expressed as (Ba et al., 2013; Chen et al., 2024a)

$$\begin{aligned}H=&\left(\frac{1}{2}\lambda_{\mathrm{u}}+\mu_{\mathrm{d}}\right)I_1^2-2\mu_{\mathrm{d}}I_2+\frac{1}{2}M\zeta^2-\alpha MI_1\zeta+\left(\frac{1}{6}\nu_1'+\nu_2'+\frac{4}{3}\nu_3'\right)I_1^3\\&+4\nu_3'I_3-(2\nu_2'+4\nu_3')I_1I_2+\gamma_1\zeta^3+\gamma_2I_1^2\zeta+\gamma_3I_1\zeta^2+\gamma I_2\zeta\end{aligned} \tag{16}$$

where $\lambda_{\mathrm{u}}=\lambda_{\mathrm{mf}}(p,\omega)+\alpha^2M$, $\mu_{\mathrm{d}}=\mu_{\mathrm{mf}}(p,\omega)$, $\alpha=1-K_{\mathrm{mf}}(p,\omega)/K_{\mathrm{gr}}$ and $M=\left[(\alpha-\phi(p))/K_{\mathrm{gr}}+\phi(p)/K_{\mathrm{f}}^{\#}(p,\omega)\right]^{-1}$ are four second-order elastic constants (2oECs). $\lambda_{\mathrm{mf}}(p,\omega)$, $\mu_{\mathrm{mf}}(p,\omega)$ and $K_{\mathrm{mf}}(p,\omega)$ are the Lamé coefficient, shear modulus and bulk modulus of stress- and frequency-dependent dry rock modified frame, respectively. K_{gr} and $K_{\mathrm{f}}^{\#}(p,\omega)$ are bulk moduli of grain and fluid, respectively. $\nu_1',\nu_2',\nu_3',\gamma_1,\gamma_2,\gamma_3,\gamma$ are seven 3oECs, in which, ν_1',ν_2',ν_3' and γ_1 are the nonlinear constants related to solid and fluid phase, respectively, γ_2,γ_3,γ are the nonlinear constants that characterize the interaction effect between solid and fluid (Liu et al., 2021). Three invariants I_1,I_2, I_3 of the strain components can be written as (Biot, 1962)

$$\begin{aligned}&I_1=E=E_{11}+E_{22}+E_{33},\\&I_2=\begin{vmatrix}E_{11}&E_{12}\\E_{12}&E_{22}\end{vmatrix}+\begin{vmatrix}E_{11}&E_{13}\\E_{13}&E_{33}\end{vmatrix}+\begin{vmatrix}E_{22}&E_{23}\\E_{23}&E_{33}\end{vmatrix},\\&I_3=\begin{vmatrix}E_{11}&E_{12}&E_{13}\\E_{21}&E_{22}&E_{23}\\E_{31}&E_{32}&E_{33}\end{vmatrix}.\end{aligned} \tag{17}$$

where E_{ij} is the solid strain expressed by the Lagrange strain tensor. According to Einstein summation convention, the expression can be represented as

$$E_{ij}=\frac{1}{2}\left(u_{i,j}+u_{j,i}+u_{k,i}u_{k,j}\right),i,j,k=1,2,3 \tag{18}$$

in which, $u_i=(u_1,u_2,u_3)$ refers to the displacement vector of the solid. $u_{i,j}$ indicates the partial derivative of displacement u_i with respect to direction $x_j=(x_1,x_2,x_3)$.

Ignoring the shear deformation of the fluid, the finite strain of the fluid under stress can be approximated as (Ba et al., 2013)

$$\zeta=-\left(w_{i,i}+\frac{1}{2}w_{i,i}^2\right),i=1,2,3 \tag{19}$$

where $w_i=\phi(p)(U_i-u_i)$, $U_i=(U_1,U_2,U_3)$ refers to the displacement vector of fluid, and $w_i=(w_1,w_2,w_3)$ represents the displacement vector of fluid relative to solid.

Under in-situ stress, the dynamic equation of the patchy-saturated porous medium can be described as the superposition of a small dynamic field generated by wave propagation onto a large static deformation state induced by the stress. Assume that the deformation induced by stress is static and homogeneous, and its magnitude is much greater than that of the wave-induced deformation (see Eq. (18) in Chen et al., 2024a).

Based on the "Small-on-Large" assumption, by substituting the strain potential energy, kinetic energy, and dissipation energy functions into the Lagrangian equation (shown in Appendix B), the dynamic equations for the patchy-saturated porous medium are derived as (Liu et al., 2021)

$$\rho\ddot{u}_i^d+\rho_{\mathrm{f}}\ddot{w}_i^d=\Theta_{ijkl}u_{k,lj}^d+\Gamma_{ij}w_{k,kj}^d \tag{20}$$

$$\rho_{\mathrm{f}}\ddot{u}_i^d+\tilde{\rho}\ddot{w}_i^d=\Gamma_{kj}u_{k,ij}^d+\Gamma w_{k,ik}^d \tag{21}$$

where $\tilde{\rho}=\tau\rho_{\mathrm{f}}/\phi(p)-\mathrm{i}\eta/(\kappa\omega)$, $\rho=[1-\phi(p)]\rho_{\mathrm{s}}+\phi(p)\rho_{\mathrm{f}}$, ρ_{s} and ρ_{f} are the density of grain and pore fluid, respectively. The mixture fluid viscosity can be calculated using $\eta=\eta^{(1)}(\eta^{(2)}/\eta^{(1)})S_2$. u^d and w^d represent the displacement of solid and relative fluid induced by wave, respectively. τ represents the tortuosity of the pore space. κ refers to the permeability of the rock. Θ_{ijkl}, Γ_{ij}, Γ_{kj} and Γ are the four coefficients of equations, displayed in Appendix B.

Substituting the plane wave solutions of solid displacement and relative fluid displacement into the dynamic equations (Eqs. (20) and (21)), the analytical expressions for the velocities of fast P-, slow P- and S-waves in patchy-saturated porous media are derived as follows (Chen et al., 2024a):

$$v_{\mathrm{P,SP}}^2=\frac{2\left(\Gamma_{33}^2-\Gamma\Theta_{3333}\right)}{-\left(\tilde{\rho}\Theta_{3333}+\rho\Gamma-2\rho_{\mathrm{f}}\Gamma_{33}\right)\pm\sqrt{\left(\tilde{\rho}\Theta_{3333}+\rho\Gamma-2\rho_{\mathrm{f}}\Gamma_{33}\right)^2-4\left(\Gamma_{33}^2-\Gamma\Theta_{3333}\right)\left(\rho_{\mathrm{f}}^2-\rho\tilde{\rho}\right)}} \tag{22}$$

$$v_{\mathrm{S}}^2=\frac{\tilde{\rho}\Theta_{1313}}{\rho\tilde{\rho}-\rho_{\mathrm{f}}^2} \tag{23}$$

with

$$\Theta_{1313}=\mu_{\mathrm{mf}}(p,\omega)-(\alpha M+\gamma/2)\zeta^s+\Big[3\lambda_{\mathrm{mf}}(p,\omega)+4\mu_{\mathrm{mf}}(p,\omega)+3\alpha^2M+\Xi_1(p)\Big]e^s, \tag{24}$$

$$\Theta_{3333}=\lambda_{\mathrm{mf}}(p,\omega)+2\mu_{\mathrm{mf}}(p,\omega)+\alpha^2M-(\alpha M-2\gamma_2)\zeta^s+\Big[5\lambda_{\mathrm{mf}}(p,\omega)+6\mu_{\mathrm{mf}}(p,\omega)+5\alpha^2M+\Xi_2(p)\Big]e^s, \tag{25}$$

$$\Gamma_{33}=\alpha M-(2\gamma_3+\alpha M)\zeta^s+(\alpha M-6\gamma_2-2\gamma)e^s, \tag{26}$$

$$\Gamma=M-3(M-2\gamma_1)\zeta^s+3(2\gamma_3+\alpha M)e^s. \tag{27}$$

where $\lambda_{\mathrm{mf}}(p,\omega)=K_{\mathrm{mf}}(p,\omega)-\frac{2}{3}\mu_{\mathrm{mf}}(p,\omega)$, $e^s=u_{1,1}^s=u_{2,2}^s=u_{3,3}^s$ denotes the static strain of the solid induced by in-situ stress, while $\zeta^s=w_{i,i}^s$ represents the static strain of the fluid. u^s and w^s represent the stress-induced displacement of solid and relative fluid, respectively. When only effective stress is considered, ζ^s and e^s can be calculated by $\zeta^s=\frac{p_{\mathrm{c}}-\alpha p_{\mathrm{f}}-3[1-\phi(p)]K_{\mathrm{mf}}(p,\omega)e^s}{3\phi(p)K_{\mathrm{mf}}(p,\omega)}$ and $e^s=\frac{p_{\mathrm{c}}-\phi(p)p_{\mathrm{f}}}{3[1-\phi(p)]K_{\mathrm{gr}}}$ (Ling et al., 2021).

Similar to Eq. (9), the approximate expressions for the 3oECs of dry rock can be written as

$$\frac{1}{\Xi_1(p)}=\frac{1}{\Xi_{1\mathrm{s}}}\left[1+\theta_{\mathrm{c}\Xi_1}\phi_{\mathrm{c}0}\exp\left(\frac{\theta_{\mathrm{c}}\phi_{\mathrm{s}0}+\theta_{\mathrm{c}}\phi_{\mathrm{s}}'-\theta_{\mathrm{c}}+1}{K_{\mathrm{drs}}}p\right)\right] \tag{28}$$

$$\frac{1}{\Xi_2(p)}=\frac{1}{\Xi_{2\mathrm{s}}}\left[1+\theta_{\mathrm{c}\Xi_2}\phi_{\mathrm{c}0}\exp\left(\frac{\theta_{\mathrm{c}}\phi_{\mathrm{s}0}+\theta_{\mathrm{c}}\phi_{\mathrm{s}}'-\theta_{\mathrm{c}}+1}{K_{\mathrm{drs}}}p\right)\right] \tag{29}$$

where $\Xi_{1\mathrm{s}}=3\nu_2'+4\nu_3'$, and $\Xi_{2\mathrm{s}}=3\nu_1'+10\nu_2'+8\nu_3'$. $\theta_{\mathrm{c}\Xi_1}$ and $\theta_{\mathrm{c}\Xi_2}$ are the SSC of the 3oECs.

Subsequently, the stress- and frequency-dependent phase velocities and inverse quality factors of P- and S-wave in patchy-saturated porous media can be calculated with

$$V_q=\left[\mathrm{Re}\left(\frac{1}{v_q(p,\omega)}\right)\right]^{-1},q=\mathrm{P,SP,S} \tag{30}$$

$$Q_q^{-1}=\frac{\mathrm{Im}\left[v_q(p,\omega)\right]}{\mathrm{Re}\left[v_q(p,\omega)\right]},q=\mathrm{P,SP,S} \tag{31}$$

where Re and Im represent the real and imaginary parts of variables in parentheses, respectively.

2.3. Wave R/T coefficient equation for patchy saturated porous media under effective stress

When an elastic wave (P-wave or S-wave, denoted with I) is incident on the interface between two half-spaces Ω_1 and Ω_2 of patchy-saturated porous media under in-situ stress, three reflected waves (P1, SP1, S1) and three transmitted waves (P2, SP2, S2) are generated, corresponding respectively to the fast P-wave, slow P-wave, and S-wave (see Fig. 2). Moreover, the non-uniform distribution of pore fluid causes elastic wave propagation to become inhomogeneous, characterized by differing propagation and attenuation directions. Accordingly, the solid displacement potential function $\Phi^{(m)}$ can be expressed as follows:

$$\Phi^{(m)}=A^{(m)}\exp\left[i\omega\left(s_1^{(m)}x_1+s_3^{(m)}x_3-t\right)\right],m=\mathrm{I,P1,SP1,S1,P2,SP2,S2} \tag{32}$$

where $s_1^{(m)}$ and $s_3^{(m)}$ represent the complex slowness in the horizontal and vertical directions, respectively. The horizontal and vertical complex slowness of incident wave are given by (Sharma, 2013; Wang et al., 2020)

$$s_1^{(\mathrm{I})}=\frac{|\mathbf{P}_0|}{\omega}\sin\vartheta_{\mathrm{I}}+i\frac{|\mathbf{A}_0|}{\omega}\sin(\vartheta_{\mathrm{I}}-\varphi_{\mathrm{I}}) \tag{33}$$

$$s_3^{(\mathrm{I})}=d_{\mathrm{Re}}^{(\mathrm{I})}+id_{\mathrm{Im}}^{(\mathrm{I})},d^{(\mathrm{I})}=pv\cdot\sqrt{(k_{\mathrm{I}}/\omega)^2-\left(s_1^{(\mathrm{I})}\right)^2} \tag{34}$$

with

$$2|\mathbf{P}_0|^2=\omega^2\left[\mathrm{Re}\left(k_{\mathrm{I}}^2/\omega^2\right)+\sqrt{\left(\mathrm{Re}\left(k_{\mathrm{I}}^2/\omega^2\right)\right)^2+\left(\mathrm{Im}\left(k_{\mathrm{I}}^2/\omega^2\right)/\cos\varphi_{\mathrm{I}}\right)^2}\right] \tag{35}$$

$$2|\mathbf{A}_0|^2=\omega^2\left[-\mathrm{Re}\left(k_{\mathrm{I}}^2/\omega^2\right)+\sqrt{\left(\mathrm{Re}\left(k_{\mathrm{I}}^2/\omega^2\right)\right)^2+\left(\mathrm{Im}\left(k_{\mathrm{I}}^2/\omega^2\right)/\cos\varphi_{\mathrm{I}}\right)^2}\right] \tag{36}$$

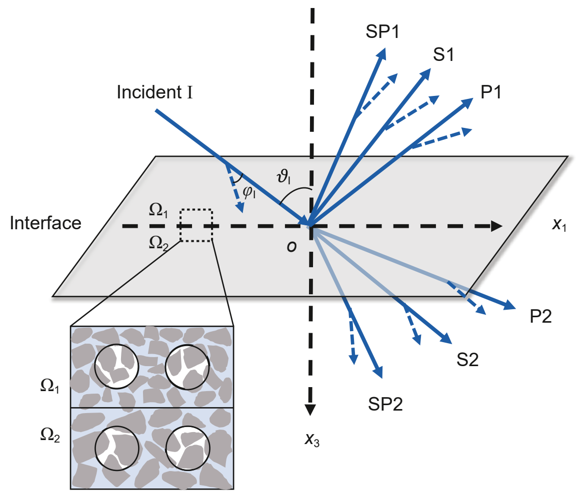

Fig. 2. Sketch of the wave reflection and transmission at the interface between two different patchy-saturated porous media. The inhomogeneity angle φ_I is defined as the angle between the attenuation direction (dashed arrows) and the propagation direction (solid arrows) of the incident wave.

where ϑ_I and φ_I refer to the angle of incidence and inhomogeneity, respectively. The symbol pv· denotes the principal value of the complex quantity $d^{(I)}$. The real and imaginary components of $d^{(I)}$ are denoted by $d_{Re}^{(I)}$ and $d_{Im}^{(I)}$. k_I represents the incident wavenumber. $|\mathbf{P}_0|$ and $|\mathbf{A}_0|$ represent the magnitudes of propagation vector and attenuation vector, respectively.

According to Snell's law, the horizontal slowness is conserved during wave reflection and transmission at an interface, as

$$s_1^{(I)} = s_1^{(P1)} = s_1^{(SP1)} = s_1^{(S1)} = s_1^{(P2)} = s_1^{(SP2)} = s_1^{(S2)} \tag{37}$$

Then, the vertical slowness of the reflected and transmitted waves can be expressed as

$$\begin{aligned} s_3^{(m)} &= -d_{Re}^{(m)} - i d_{Im}^{(m)}, d^{(m)} = pv\cdot\sqrt{(k_m/\omega)^2 - \left(s_1^{(m)}\right)^2}, m = P1, SP1, S1, \\ s_3^{(m)} &= d_{Re}^{(m)} + i d_{Im}^{(m)}, d^{(m)} = pv\cdot\sqrt{(k_m/\omega)^2 - \left(s_1^{(m)}\right)^2}, m = P2, SP2, S2. \end{aligned} \tag{38}$$

Assuming $\Re = 1$ for P-wave incidence and $\Re = 0$ for S-wave incidence, the solid displacements of Ω_1 and Ω_2 half-spaces are respectively given by

$$\mathbf{u}^{(1)} = \Re\nabla\Phi^{(I)} + \nabla\Phi^{(P1)} + \nabla\Phi^{(SP1)} + (1-\Re)\nabla\times\Phi^{(I)} + \nabla \times \Phi^{(S1)} \tag{39}$$

$$\mathbf{u}^{(2)} = \nabla\Phi^{(P2)} + \nabla\Phi^{(SP2)} + \nabla\times\Phi^{(S2)} \tag{40}$$

Considering that the relative fluid-solid displacement of fast P-wave and S-wave can be neglected, while the fluid relative displacement of the slow P-wave is coupled with the solid phase. Therefore, the relative fluid displacements in the Ω_1 and Ω_2 half-spaces can be expressed as (Geertsma and Smit, 1961)

$$\mathbf{w}^{(1)} = \xi^{(1)}\nabla\Phi^{(SP1)} \tag{41}$$

$$\mathbf{w}^{(2)} = \xi^{(2)}\nabla\Phi^{(SP2)} \tag{42}$$

with

$$\xi^{(n)} = -\frac{K_{mf}(p,\omega) + 4\big/3\mu_{mf}(p,\omega) + \alpha^2 M}{\alpha M}, n = 1,2 \tag{43}$$

Under the open-pore assumption at the interface, the boundary conditions at $x_3 = 0$ are given as follows:

(a) The solid displacement is continuous in the x_1 direction

$$u_1^{(1)} = u_1^{(2)} \tag{44}$$

(b) The solid displacement is continuous in the x_3 direction

$$u_3^{(1)} = u_3^{(2)} \tag{45}$$

(c) The total normal stress in the solid phase is continuous

$$\sigma_{33}^{(1)} = \sigma_{33}^{(2)} \tag{46}$$

(d) The total shear stress in the solid phase is continuous

$$\sigma_{13}^{(1)} = \sigma_{13}^{(2)} \tag{47}$$

(e) The relative fluid displacement is continuous in the x_3 direction

$$w_3^{(1)} = w_3^{(2)} \tag{48}$$

(f) The fluid pressure is continuous in the x_3 direction

$$p_f^{(1)} = p_f^{(2)} \tag{49}$$

By substituting the solid and fluid displacements in the upper and lower half-spaces from Eqs. (39)–(42), together with the solid and fluid constitutive relationship of the patchy-saturated porous media model (see Appendix C), into the boundary conditions specified in Eqs. (44)–(49), the function for the complex amplitude ratios of displacement potential is derived as (see Fig. 3)

$$\mathbf{Gx} = \mathbf{B} \tag{50}$$

where

$\mathbf{x} = [x_m] = \left[A^{(m)}/A^{(I)}\right] = |x_m|\exp(i\psi_m), m = P1, SP1, S1, P2, SP2, S2$

denote the reflection and transmission coefficients (R/T coefficients) expressed in terms of the complex amplitude ratios of displacement potential. ψ_m refers to the phase angles of the reflected and transmitted waves. The detailed expressions of the coefficient matrix $\mathbf{G}$ and the vector $\mathbf{B}$ are provided in Appendix D. Based on Eq. (50), the R/T coefficients for fast P-wave, slow P-wave and S-wave in terms of displacement amplitude ratio can be further obtained as

$$R_{Pm} = |R_{Pm}|\exp(i\psi_{m1}) = \frac{A^{(m1)}k_{m1}}{A^{(I)}k_I} \tag{51}$$

$$T_{Pm} = |T_{Pm}|\exp(i\psi_{m2}) = \frac{A^{(m2)}k_{m2}}{A^{(I)}k_I}, m = P, SP, S \tag{52}$$

where, $|R_{Pm}|$ and $|T_{Pm}|$ represent the absolute values of the complex reflection and transmission coefficients, respectively.

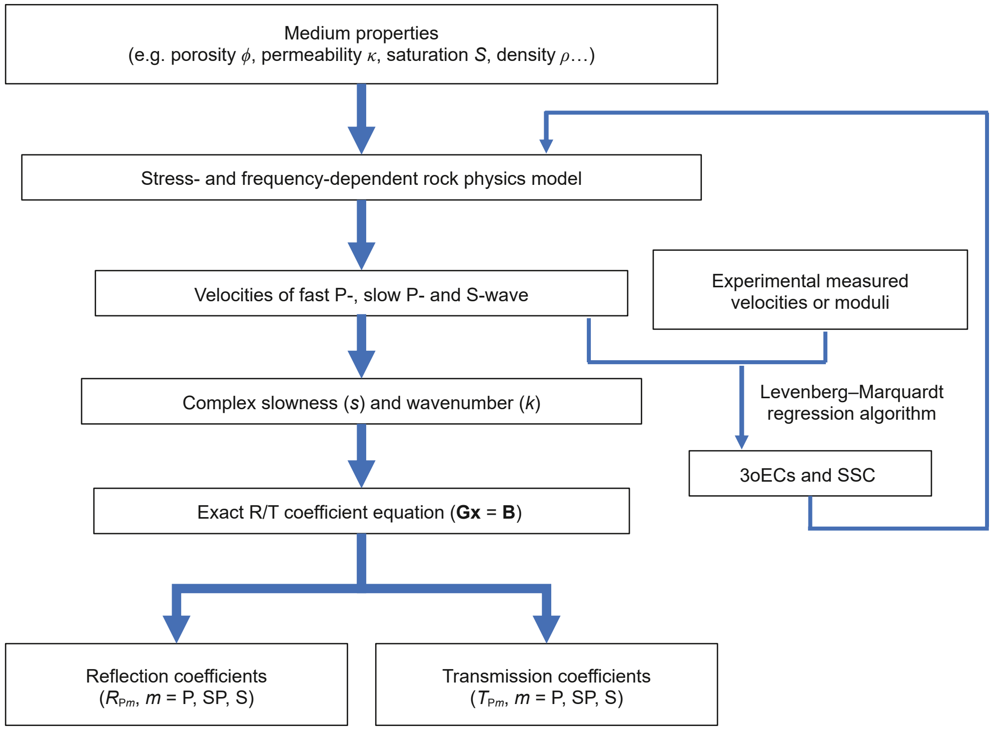

Fig. 3. Flowchart for calculating reflection and transmission coefficients at the interface between two patchy-saturated porous media.

2.4. Energy partitions

For a unit-area surface element at the interface between Ω_1 and Ω_2, the energy flux across the surface can be expressed as the scalar product of the surface traction and particle velocity (Kumar et al., 2018; Sharma, 2013; Wang et al., 2020). Based on the stress- and frequency-dependent multiscale rock physics theory proposed above, the averaged energy intensity of a wave at x_3= 0 is given by

$$L=\frac{1}{2}\mathrm{Re}\left\{\sigma_{33}\bar{\dot{u}}_3+\sigma_{13}\bar{\dot{u}}_1-p_\mathrm{f}\bar{\dot{w}}_3\right\} \tag{53}$$

where the bar denotes conjugate of the complex quantity. The energy fluxes of the four waves (one incident and three reflected) and their interactions in the medium can be represented by the following fourth-order matrix

$$\mathbf{L}_{\Omega_1}=\begin{bmatrix} L_{00} & L_{01} & L_{02} & L_{03}\\ L_{10} & L_{11} & L_{12} & L_{13}\\ L_{20} & L_{21} & L_{22} & L_{23}\\ L_{30} & L_{31} & L_{32} & L_{33}\end{bmatrix}=\frac{1}{2}\mathrm{Re}\left\{\mathbf{J}^i_{4\times3}\bar{\mathbf{Y}}^i_{3\times4}\right\} \tag{54}$$

with

$$\mathbf{J}^i_{4\times3}=\begin{bmatrix} \sigma_{33}^{(\mathrm{I})} & \sigma_{13}^{(\mathrm{I})} & -p_\mathrm{f}^{(\mathrm{I})}\\ \sigma_{33}^{(\mathrm{P1})} & \sigma_{13}^{(\mathrm{P1})} & -p_\mathrm{f}^{(\mathrm{P1})}\\ \sigma_{33}^{(\mathrm{SP1})} & \sigma_{13}^{(\mathrm{SP1})} & -p_\mathrm{f}^{(\mathrm{SP1})}\\ \sigma_{33}^{(\mathrm{S1})} & \sigma_{13}^{(\mathrm{S1})} & -p_\mathrm{f}^{(\mathrm{S1})}\end{bmatrix}=\omega^2\begin{bmatrix} -A^{(\mathrm{I})}b_3 & -A^{(\mathrm{I})}b_4 & A^{(\mathrm{I})}b_6\\ A^{(\mathrm{P1})}G_{31} & A^{(\mathrm{P1})}G_{41} & -A^{(\mathrm{P1})}G_{61}\\ A^{(\mathrm{SP1})}G_{32} & A^{(\mathrm{SP1})}G_{42} & -A^{(\mathrm{SP1})}G_{62}\\ A^{(\mathrm{S1})}G_{33} & A^{(\mathrm{S1})}G_{43} & -A^{(\mathrm{S1})}G_{63}\end{bmatrix} \tag{55}$$

$$\mathbf{Y}^i_{3\times4}=\begin{bmatrix} \dot{u}_3^{(\mathrm{I})} & \dot{u}_3^{(\mathrm{P1})} & \dot{u}_3^{(\mathrm{SP1})} & \dot{u}_3^{(\mathrm{S1})}\\ \dot{u}_1^{(\mathrm{I})} & \dot{u}_1^{(\mathrm{P1})} & \dot{u}_1^{(\mathrm{SP1})} & \dot{u}_1^{(\mathrm{S1})}\\ \dot{w}_3^{(\mathrm{I})} & \dot{w}_3^{(\mathrm{P1})} & \dot{w}_3^{(\mathrm{SP1})} & \dot{w}_3^{(\mathrm{S1})}\end{bmatrix}=\omega^2\begin{bmatrix} -A^{(\mathrm{I})}b_2 & A^{(\mathrm{P1})}G_{21} & A^{(\mathrm{SP1})}G_{22} & A^{(\mathrm{S1})}G_{23}\\ -A^{(\mathrm{I})}b_1 & A^{(\mathrm{P1})}G_{11} & A^{(\mathrm{SP1})}G_{12} & A^{(\mathrm{S1})}G_{13}\\ -A^{(\mathrm{I})}b_5 & A^{(\mathrm{P1})}G_{51} & A^{(\mathrm{SP1})}G_{52} & A^{(\mathrm{S1})}G_{53}\end{bmatrix} \tag{56}$$

where L_{00}, L_{11}, L_{22} and L_{33} denote the energy fluxes of incident wave (I) and three reflected waves (P1, SP1, S1), respectively, while the other terms represent the interference energy fluxes between these waves. The detailed expressions of b_n and G_{nm} are given in Appendix D.

Similarly, the energy fluxes corresponding to the three transmitted waves in medium Ω_2 can be represented as

$$\mathbf{L}_{\Omega_2} = \begin{bmatrix} L_{44} & L_{45} & L_{46} \\ L_{54} & L_{55} & L_{56} \\ L_{64} & L_{65} & L_{66} \end{bmatrix} = \frac{1}{2}\mathrm{Re}\left\{\mathbf{J}^t_{3\times3}\overline{\mathbf{Y}}^t_{3\times3}\right\} \tag{57}$$

with

$$\mathbf{J}^t_{3\times3} = \begin{bmatrix} \sigma_{33}^{(\mathrm{P2})} & \sigma_{13}^{(\mathrm{P2})} & -p_{\mathrm{f}}^{(\mathrm{P2})} \\ \sigma_{33}^{(\mathrm{SP2})} & \sigma_{13}^{(\mathrm{SP2})} & -p_{\mathrm{f}}^{(\mathrm{SP2})} \\ \sigma_{33}^{(\mathrm{S2})} & \sigma_{13}^{(\mathrm{S2})} & -p_{\mathrm{f}}^{(\mathrm{S2})} \end{bmatrix} = \omega^2 \begin{bmatrix} -A^{(\mathrm{P2})}G_{34} & -A^{(\mathrm{P2})}G_{44} & A^{(\mathrm{P2})}G_{64} \\ -A^{(\mathrm{SP2})}G_{35} & -A^{(\mathrm{SP2})}G_{45} & A^{(\mathrm{SP2})}G_{65} \\ -A^{(\mathrm{S2})}G_{36} & -A^{(\mathrm{S2})}G_{46} & A^{(\mathrm{S2})}G_{66} \end{bmatrix} \tag{58}$$

$$\mathbf{Y}^t_{3\times3} = \begin{bmatrix} \dot{u}_3^{(\mathrm{P2})} & \dot{u}_3^{(\mathrm{SP2})} & \dot{u}_3^{(\mathrm{S2})} \\ \dot{u}_1^{(\mathrm{P2})} & \dot{u}_1^{(\mathrm{SP2})} & \dot{u}_1^{(\mathrm{S2})} \\ \dot{w}_3^{(\mathrm{P2})} & \dot{w}_3^{(\mathrm{SP2})} & \dot{w}_3^{(\mathrm{S2})} \end{bmatrix} = \omega^2 \begin{bmatrix} -A^{(\mathrm{P2})}G_{24} & -A^{(\mathrm{SP2})}G_{25} & -A^{(\mathrm{S2})}G_{26} \\ -A^{(\mathrm{P2})}G_{14} & -A^{(\mathrm{SP2})}G_{15} & -A^{(\mathrm{S2})}G_{16} \\ -A^{(\mathrm{P2})}G_{54} & -A^{(\mathrm{SP2})}G_{55} & -A^{(\mathrm{S2})}G_{56} \end{bmatrix} \tag{59}$$

where L_{44}, L_{55} and L_{66} denote the energy fluxes of three transmitted waves (P2, SP2, S2), while the other terms represent the interference energy fluxes between these waves.

Taking the direction of the incident energy flux as positive, the total energy at $x_3 = 0$ can be computed from the following formula, which is consistent with the principle of total energy conservation

$$RA_{\mathrm{sum}} = \sum_{m=1}^{3}\frac{L_{mm}}{L_{00}} + RA_{\mathrm{ir}} - \sum_{m=4}^{6}\frac{L_{mm}}{L_{00}} - RA_{\mathrm{tt}} = -1 \tag{60}$$

where RA_{ir} represents the interference contribution to the reflected energy flux, including the interaction between the incident and reflected waves as well as the mutual interference among the reflected waves. RA_{tt} denotes the interference contribution arising from the transmitted waves. Both quantities can be calculated using the following expressions

$$RA_{\mathrm{ir}} = \sum_{m=1}^{3}\frac{L_{m0}+L_{0m}}{L_{00}} + \sum_{m=1}^{3}\left(\sum_{n=1}^{3}\frac{L_{mn}}{L_{00}} - \frac{L_{mm}}{L_{00}}\right) \tag{61}$$

$$RA_{\mathrm{tt}} = \sum_{m=4}^{6}\left(\sum_{n=4}^{6}\frac{L_{mn}}{L_{00}} - \frac{L_{mm}}{L_{00}}\right) \tag{62}$$

3. Results and analysis

3.1. Wave velocity dispersion and attenuation in patchy-saturated porous media

Based on the rock physics model of patchy-saturated porous media established above, numerical simulations are performed to investigate the dispersion and attenuation characteristics of fast P-, slow P-, and S-wave velocities as functions of frequency and effective stress. The model parameters used in the simulations are summarized in Table 1 (Medium I), and corresponding results are presented in Fig. 4.

As shown in Fig. 4, with increasing frequency, the fast P-wave velocity exhibits three successive attenuation peaks, corresponding respectively to wave dispersion and attenuation caused by mesoscopic fluid patchy saturation, microscopic squirt flow, and macroscopic global flow. In contrast, S-wave velocity displays only two attenuation peaks at the microscopic and macroscopic scales. This behavior arises from the assumption that the fluid shear modulus is zero, implying that variations in fluid content do not influence the shear deformation of the rock (White, 1975). Additionally, it is assumed that fluid patches maintain a spherical shape under compressional wave excitation, while the asymmetric oscillation induced by shear wave is neglected (Shi et al., 2024). As the effective stress increases, the fast P- and S-wave velocities

Table 1
Parameter value settings for the patchy-saturated porous media.

Parameter	Medium I	Medium II	Parameter	Medium I	Medium II
Grain bulk modulus K_{gr}, GPa	38	28	Crack aspect ratio β	0.004	0.004
Grain density ρ_{s}, kg/m^3	2650	2250	Permeability κ, mD	1	1
Initial stiff porosity ϕ_{s0}	0.2	0.2	Tortuosity τ	2	2
Initial compliant porosity ϕ_{c0}	0.003	0.003	Inner sphere radius a, mm	2	2
Dry bulk modulus K_{drs}, GPa	20.8	8.8	Outer sphere radius b, mm	7	7
Dry shear modulus μ_{drs}, GPa	26.2	12.2	Modulus SSC $\theta_{\mathrm{c}}/\theta_{\mathrm{c\mu}}$	310.6/302.5	310.6/302.5
Fluid bulk modulus[a] $K_{\mathrm{f}}^{(\mathrm{gas})}/K_{\mathrm{f}}^{(\mathrm{water})}$, GPa	0.0022/2.2	0.0022/2.2	3oEC SSC[b] $\theta_{\mathrm{c}\Xi_1}/\theta_{\mathrm{c}\Xi_2}$	0/0	0/0
Fluid density[a] $\rho_{\mathrm{f}}^{(\mathrm{gas})}/\rho_{\mathrm{f}}^{(\mathrm{water})}$, kg/m^3	10.8/1031	10.8/1031	3oEC[b] $\Xi_{1\mathrm{s}}/\Xi_{2\mathrm{s}}$, GPa	240/3000	240/3000
Fluid viscosity coefficient[a] $\eta^{(\mathrm{gas})}/\eta^{(\mathrm{water})}$, Pa·s	0.00011 /0.001	0.00011 /0.001	3oEC[b] $\gamma/\gamma_1/\gamma_2/\gamma_3$, GPa	−450/−0.12 /−10/−1.9	−450/−0.12 /−10/−1.9

[a] Data from Gurevich et al. (2010).
[b] Data from Chen et al. (2024a).

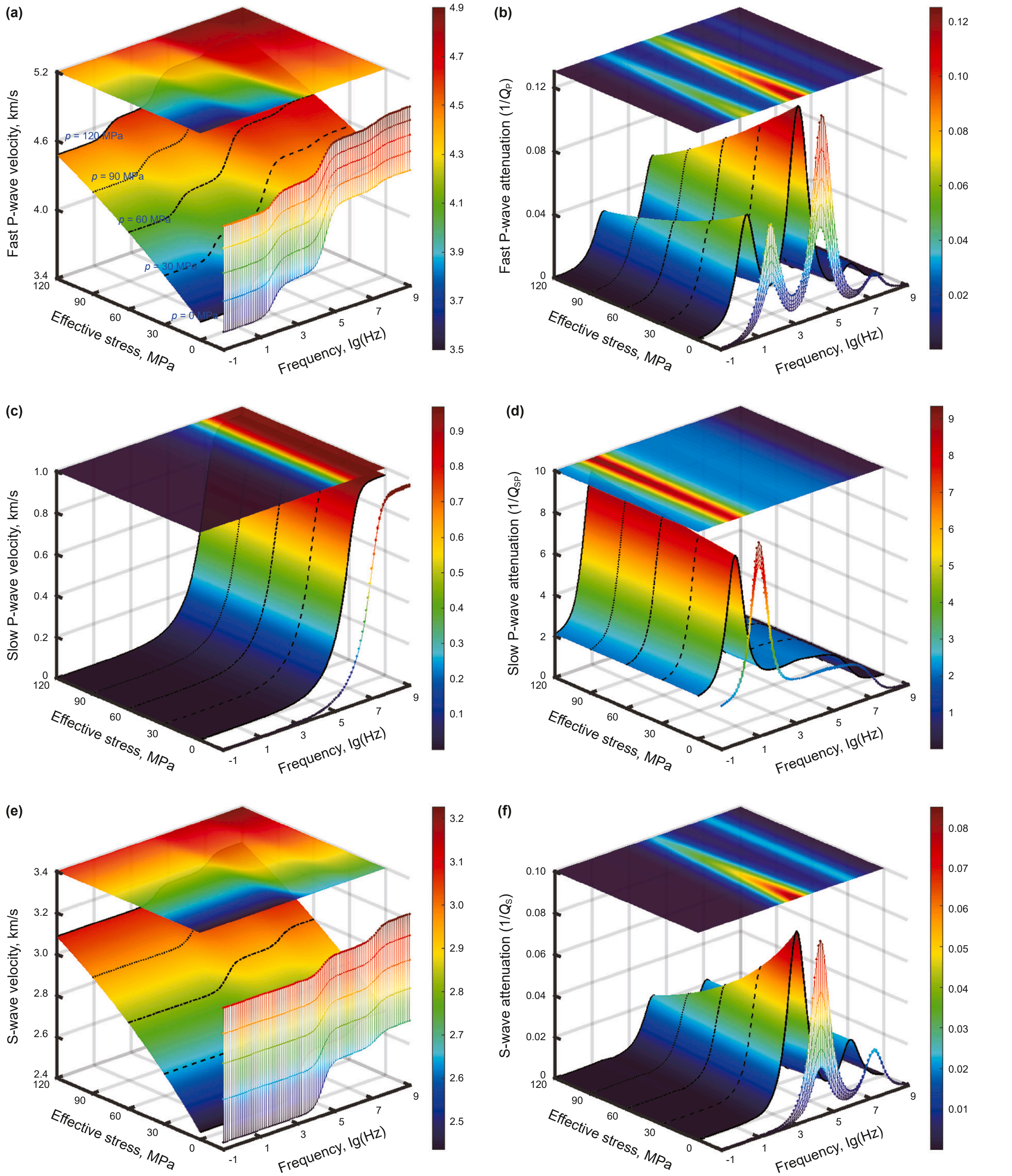

Fig. 4. Fast P-wave (**a**), slow P-wave (**c**) and S-wave (**e**) velocities, along with the corresponding attenuation factors ((**b**), (**d**) and (**f**)), as functions of frequency and effective stress for patchy-saturated porous media. Curves extracted at effective stresses of 0, 30, 60, 90, and 120 MPa are shown for comparison.

increase, while their dispersion and attenuation decrease. This is primarily due to the closure of compliant cracks in the porous rock, which significantly increases rock stiffness and reduces the squirt flow interaction between the cracks and stiff pores. Meanwhile, the impact of effective stress on velocity variations is markedly reduced at high frequencies compared with low frequencies. This is because the rock remains unrelaxed at high frequencies, which reduces its sensitivity to stress. Unlike fast P- and S-waves, slow P-wave velocity rises noticeably only at high frequencies, with effective stress variations exerting minimal influence.

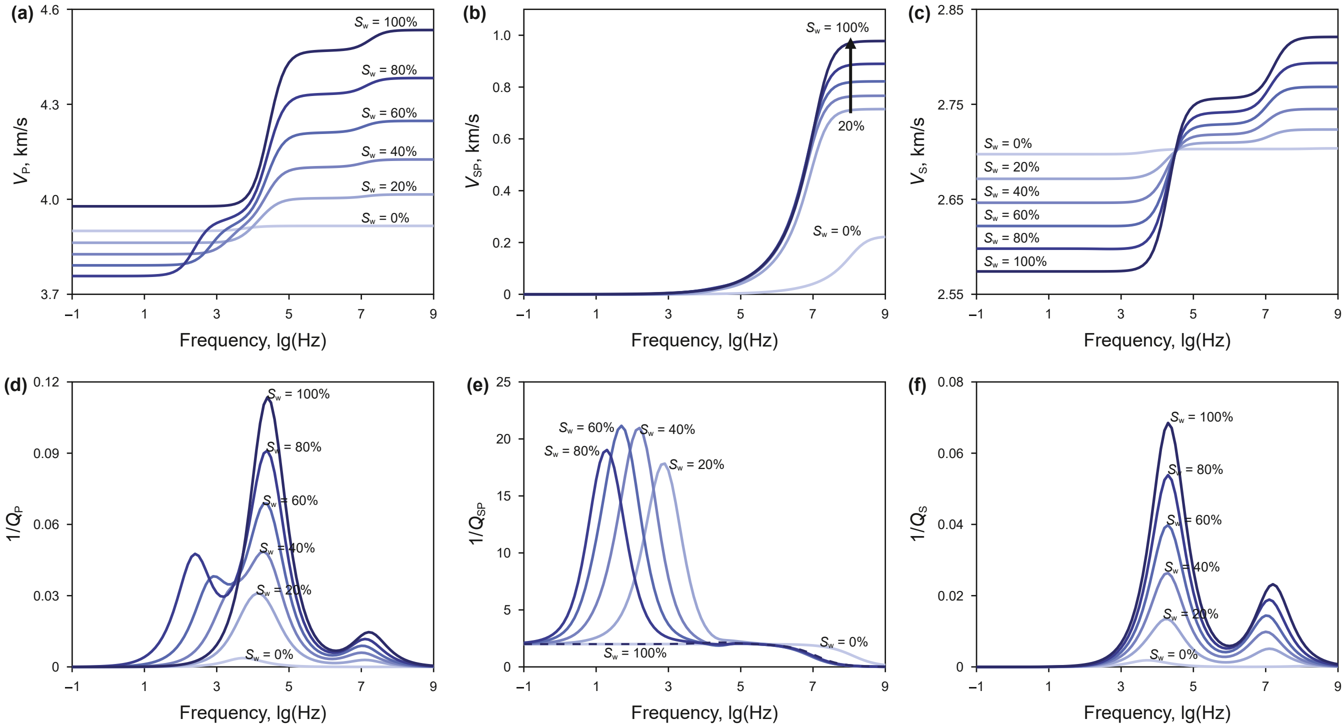

Fig. 5. Fast P-wave **(a)**, slow P-wave **(b)** and S-wave **(c)** velocities, along with the corresponding attenuation factors **(d)**–**(f)**, as a function of frequency under different water saturations and an effective stress of 20 MPa.

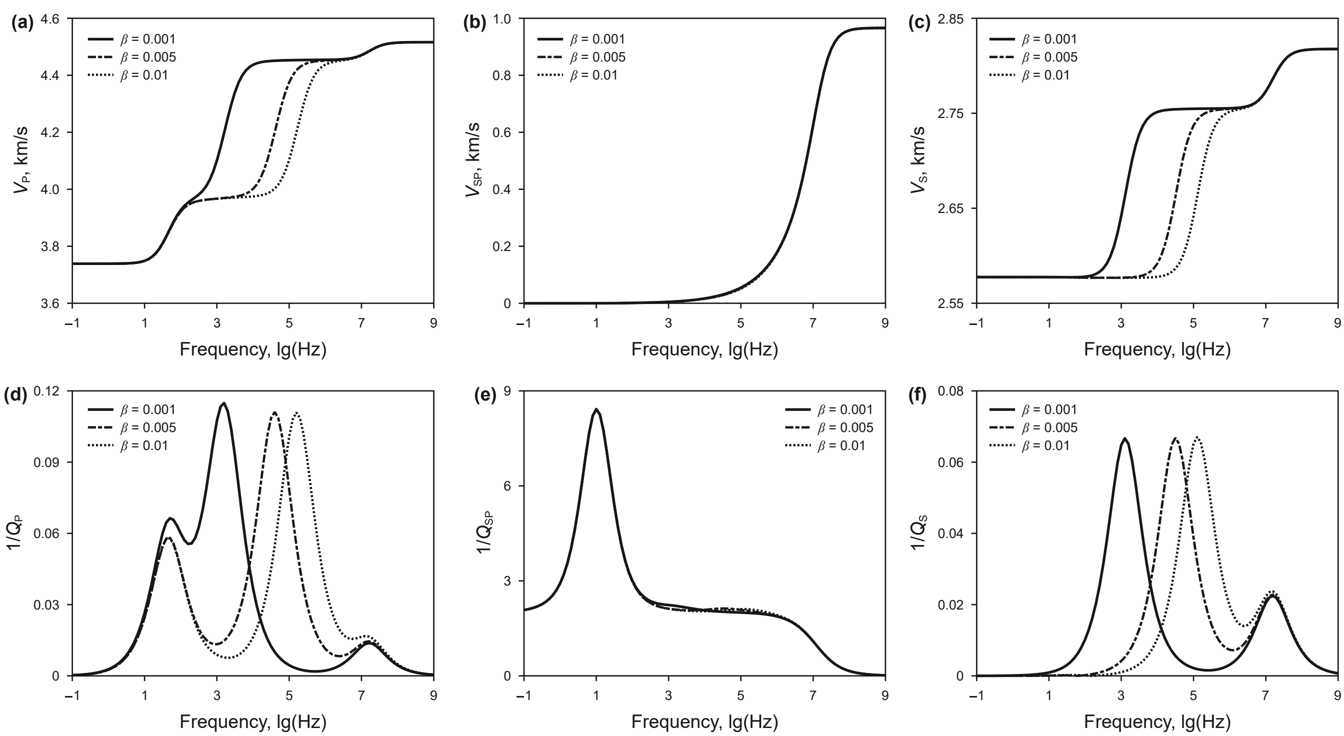

Fig. 6. Fast P-wave **(a)**, slow P-wave **(b)** and S-wave **(c)** velocities, along with the corresponding attenuation factors **(d)**–**(f)**, as a function of frequency under different crack aspect ratios and an effective stress of 20 MPa.

Furthermore, to investigate the influence of water saturation variations on velocity dispersion and attenuation in patchy-saturated porous media, numerical simulations of fast P-, slow P-, and S-wave velocities are conducted as a function of frequency under different water saturations at an effective stress of 20 MPa, as shown in Fig. 5. At low frequencies, the fast P-wave velocity decreases with increasing water saturation, while mesoscale dispersion and attenuation become more pronounced. Compared

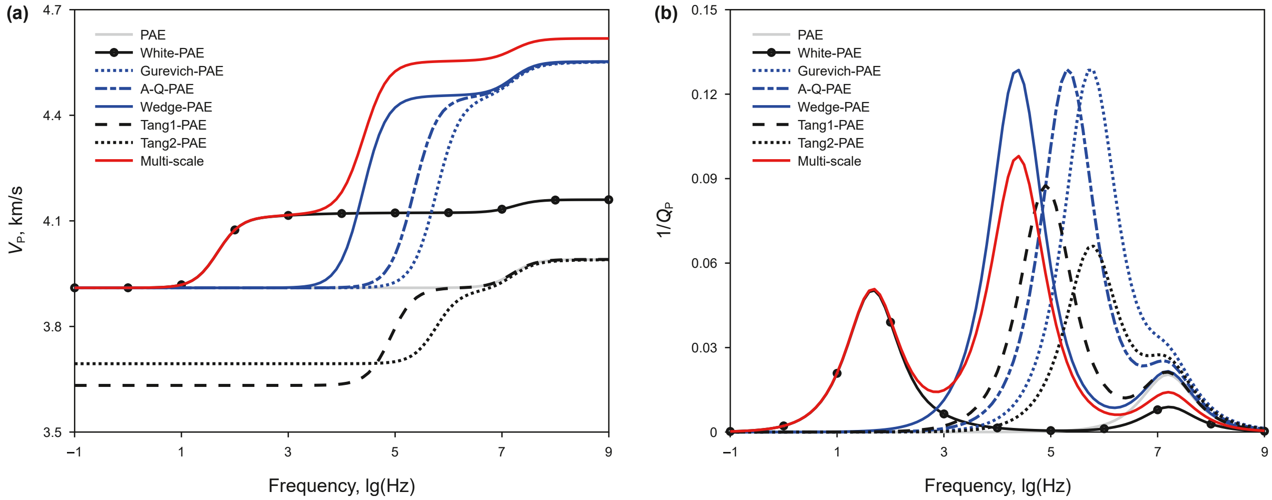

Fig. 7. Comparison of the fast P-wave velocity dispersion **(a)** and attenuation **(b)** predicted by the proposed multi-scale model (red), with several classical models incorporating PAE theory under an effective stress of 40 MPa Chen et al. (2024a). "White" denotes the patchy-saturation model (White, 1975); "Gurevich", "A-Q", "Tang1", and "Tang2" denote the disk-shaped squirt-flow models of Gurevich et al. (2010), Alkhimenkov and Quintal (2024), Tang (2011), and Tang et al. (2012), respectively; "Wedge" denotes the wedge-shaped squirt-flow model of Chen et al. (2025).

with media saturated by a single fluid, patchy-saturated media exhibit a shift of the dispersion characteristic frequency toward lower values. This behavior is mainly attributed to diffusive processes at the patch scale, which require a longer relaxation time. When water saturation reaches 100%, mesoscale dispersion and attenuation vanish, and the fast P-wave velocity becomes relatively high. This phenomenon arises because water possesses a higher bulk modulus and viscosity than gas, which increases the stiffness of the rock. In contrast, at both micro- and macro-scales, velocity dispersion and attenuation increase progressively with rising water saturation, causing fast P-wave velocity to exhibit a continuous upward trend at high frequencies. As described above, the S-wave velocity exhibits no attenuation at the mesoscopic scale. Consequently, under the combined effects of microscale squirt flow and macroscale global flow, S-wave velocity decreases at low frequencies but increases at high frequencies with rising water saturation. Compared with effective stress, water saturation has a more pronounced effect on the variation of slow P-wave velocity.

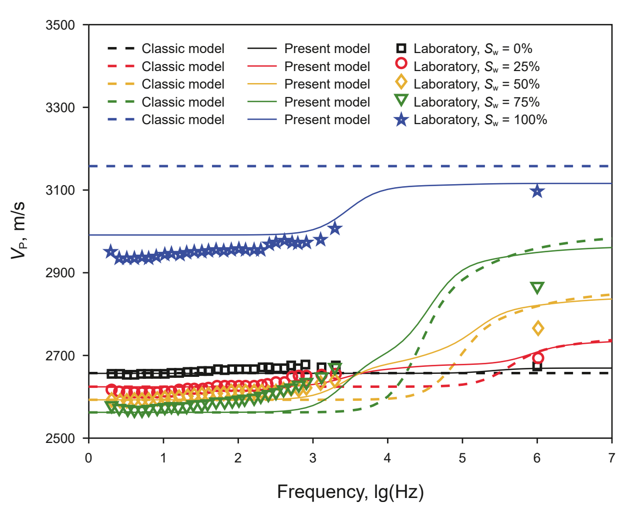

Fig. 8. Comparison of fast P-wave velocities computed by our new model (solid lines) and classical White's model (dashed lines) with experimental data (markers) for a sandstone sample from Ma et al. (2018) under different water saturations.

Then we analyze the effect of crack aspect ratio β on the wave dispersion and attenuation in patchy-saturated porous media with wedge-shaped cracks, as shown in Fig. 6. The figure shows that the dispersion and attenuation of fast P-wave and S-wave velocities vary significantly with changes in the crack aspect ratio, whereas the slow P-wave velocity is less affected. The crack aspect ratio primarily affects velocity at the microscale, leading to a shift of the dispersion characteristic frequency toward higher values as the crack aspect ratio increases.

Fig. 7 presents a comparison of fast P-wave velocity dispersion and attenuation calculated using our new multiscale model with those obtained from several previously published models under an effective stress of 40 MPa. These models include a macroscale PAE model (Chen et al., 2024a), as well as mesoscale patchy-saturation (White, 1975) and microscale squirt-flow models (Alkhimenkov and Quintal, 2024; Chen et al., 2025; Gurevich et al., 2010; Tang, 2011; Tang et al., 2012) that incorporate PAE theory. The comparison reveals that our proposed multiscale model agrees well with the PAE model at lower frequencies. With increasing frequency, velocity dispersion and attenuation arise due to mesoscopic fluid patchy saturation and microscopic squirt-flow mechanisms. At higher frequencies, a minor relaxation peak is observed, corresponding to the energy dissipation governed by the PAE mechanism. Furthermore, the predicted fast P-wave velocity dispersion and attenuation exhibit good consistency with previously developed single- and double-scale WIFF models across their dominant frequency ranges. The relative increase or decrease in attenuation predicted by the multiscale model may arise from interactions among different fluid-flow mechanisms. The results indicate that our multiscale model effectively characterizes wave dispersion and attenuation across a broader frequency range.

To further demonstrate the validity of our new model, two sets of previously published experimental data are selected for verification, as shown in Figs. 8 and 9. Fig. 8 shows the comparison of fast P-wave velocities computed by our new model, classical White's model (White, 1975; Dutta and Seriff, 1979) with experimental data. The experimental sample shown in the figure is a partially saturated sandstone containing both gas and water (Ma et al., 2018). Experimental measurements are conducted on the

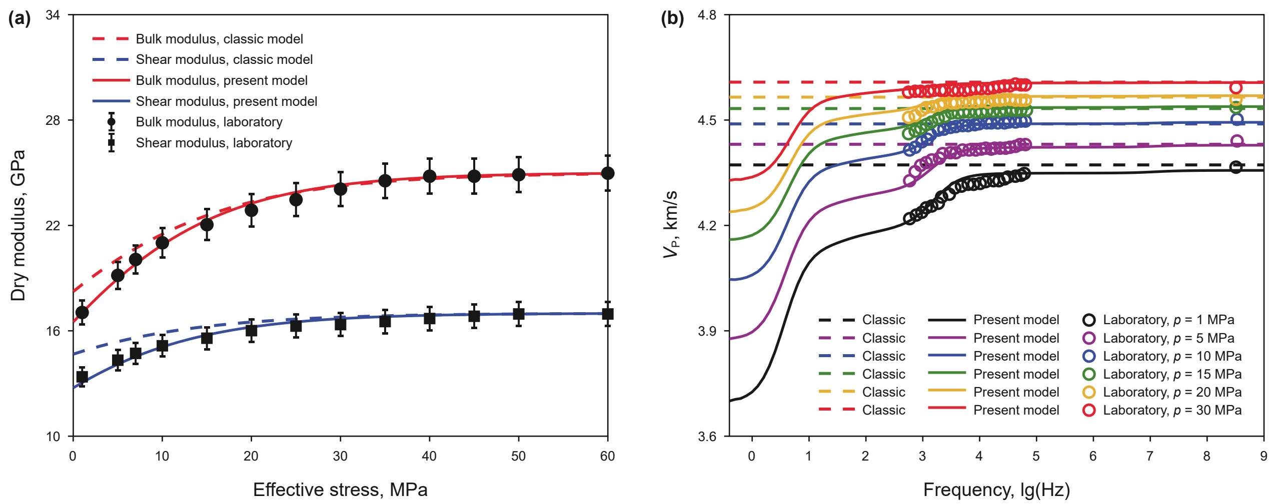

Fig. 9. Comparison of predictions from our new model (solid lines) and classical Chen's PAE model (dashed lines) with experimental data for tight sandstone sample A from He et al. (2024a) under different effective stresses: **(a)** dry bulk modulus (circles) and dry shear modulus (squares); **(b)** fast P-wave velocity (circles). The error bars indicate ±4% errors.

Table 2
Properties of the rock samples.

Properties	Sandstone[a]	Tight sandstone A[b]	Tight sandstone B[b]
Mineral composition, %	Quartz: 33.8 K-feldspar: 8.3 Plagioclase: 41.4 Clay: 5.8 Dolomite: 10.7	Quartz: 79.5 Calcite: 4.3 Feldspar: 8.04 Clay: 5.3 Muscovite: 2.86	Quartz: 72.5 Calcite: 4.5 Feldspar: 15.8 Clay: 4.7 Muscovite: 2.5
Grain bulk modulus, GPa	58	41.5	Voigt-Reuss-Hill average (Hill, 1952)
Density, kg/m^3	2600	2440	2340
Porosity	0.2054	0.0793	0.0851
Permeability, mD	116.27	0.063	0.026
Saturation, %	Vary	Glycerine: 90 Gas: 10	Brine: 40 Gas: 60
Fluid bulk modulus, GPa	Water: 2.25 Air: 0.0001011	Glycerine: 4.586 Gas: 0.00136	Brine: 2.28 Gas: 0.00136
Fluid density, kg/m^3	Water: 997 Air: 1.17	Glycerine: 1252.2 Gas: 11.5	Brine: 1013 Gas: 11.5
Fluid viscosity coefficient, Pa·s	Water: 0.0010087 Air: 0.000015	Glycerine: 1.410063 Gas: 0.0000172	Brine: 0.0010226 Gas: 0.0000172

[a] Data from Ma et al. (2018) and Jiang et al. (2025).
[b] Data from He et al. (2024a).

rock sample within the seismic (2–2000 Hz) and ultrasonic frequencies (1 MHz) under confining pressure of 40 MPa and room temperature of approximately 23 °C, with water saturations of 0%, 25%, 50%, 75%, and 100%. The specific physical parameters of the rock samples are summarized in Table 2 (Jiang et al., 2025; Ma et al., 2018). Since crack-related parameters (e.g., crack porosity and SSC) are neither experimentally measured nor explicitly defined, they are treated as fitting parameters and determined using the Levenberg–Marquardt regression algorithm (Levenberg, 1944; Marquardt, 1963). As shown in the figure, at low frequencies, the fast P-wave velocity decreases with increasing water saturation, while it reaches a relatively high value when the water saturation is 100%. At high frequencies, the fast P-wave velocity increases continuously as water saturation increases. This trend is consistent with the result of the previous numerical simulation (see Fig. 5(a)). In addition, the comparison shows that the velocity predicted by the classical White model deviates significantly from the experimental data at full water saturation. This is because the model only accounts for mesoscopic wave dispersion and attenuation caused by multiphase fluids, whereas in real rocks, the squirt flow between pores and cracks also cannot be ignored. By contrast, our new model shows good agreement with the experimental data across a wide range of frequencies and water saturations, thereby validating the reasonableness of the proposed model.

Fig. 9 illustrates a set of experimental data from a tight sandstone sample A under varying effective stress, with the data provided by He et al. (2024a). The corresponding physical properties of the rock sample are detailed in Table 2. Fig. 9(a) compares the predictions from our new model and classical PAE model (Chen et al., 2024a) with experimental measurements of the dry rock bulk and shear moduli as functions of effective stress. It can be observed that, as effective stress increases, the moduli of the dry rock initially increase nonlinearly and then gradually level off. This behavior is attributed to the rapid closure of compliant cracks under stress. At higher effective stresses, once the cracks are fully closed, the subsequent linear increase in moduli is primarily governed by the stiff porosity and the finite deformation of the rock. Compared with the classical PAE model, our new model provides a better interpretation of the experimental measurements over a wider effective stress range. Subsequently, the model predictions are compared with experimental measurements of

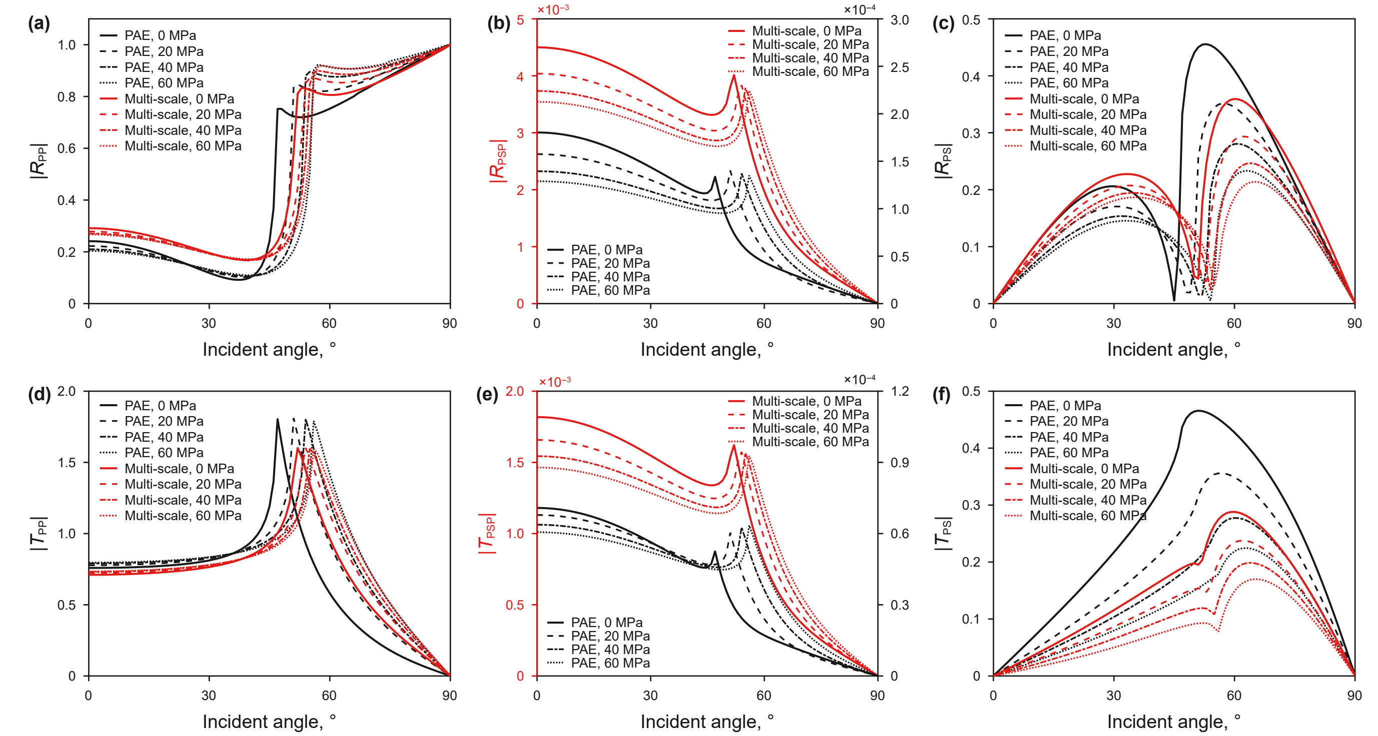

Fig. 10. R/T coefficients of fast P-wave (**a, d**), slow P-wave (**b, e**) and S-wave (**c, f**) at the interface between two patchy-saturated porous media, as a function of incidence angle (frequency = 1 MHz, inhomogeneity angle = 45°) under different effective stresses. Results from the proposed multiscale model are compared with Chen's PAE model.

partially glycerine and gas saturated samples under varying frequencies and effective stresses. The results indicate that the extent of P-wave velocity dispersion decreases as the effective stress increases. Moreover, unlike the classical PAE model, which agrees well with the experimental data only at high frequencies, our model predicts P-wave velocities that show good agreement with the experimental data in both the well-logging and ultrasonic frequency ranges. These results further validate the effectiveness of our proposed stress- and frequency-dependent rock physics model.

3.2. Wave R/T coefficients at the interface between two patchy-saturated porous media

To further investigate the reflection and transmission (R/T) characteristics of elastic P-waves at the interface of patchy-saturated porous media under effective stress, numerical analyses of the R/T coefficients for fast P-, slow P- and S-waves are performed using our new rock physics model established above. In this study, patchy-saturated porous medium II is defined as the upper half-space Ω_1, and patchy-saturated porous medium I as the lower half-space medium Ω_2. The corresponding material parameters are provided in Table 1.

Fig. 10 illustrates the variations of wave R/T coefficients with incident angle and effective stress at a frequency of 1 MHz and an inhomogeneity angle of 45°. As shown in the figure, no S-wave is generated when the inhomogeneous plane wave is normally incident. With increasing effective stress, the amplitude of the fast P-wave reflection coefficient decreases, while that of the transmission coefficient increases. In contrast, both the R/T magnitudes of the slow P-wave decrease. This trend is likely attributed to the closure of cracks in the upper and lower media with increasing effective stress, which enhances rock stiffness and simultaneously reduces the velocity contrast between the two layers. In addition,

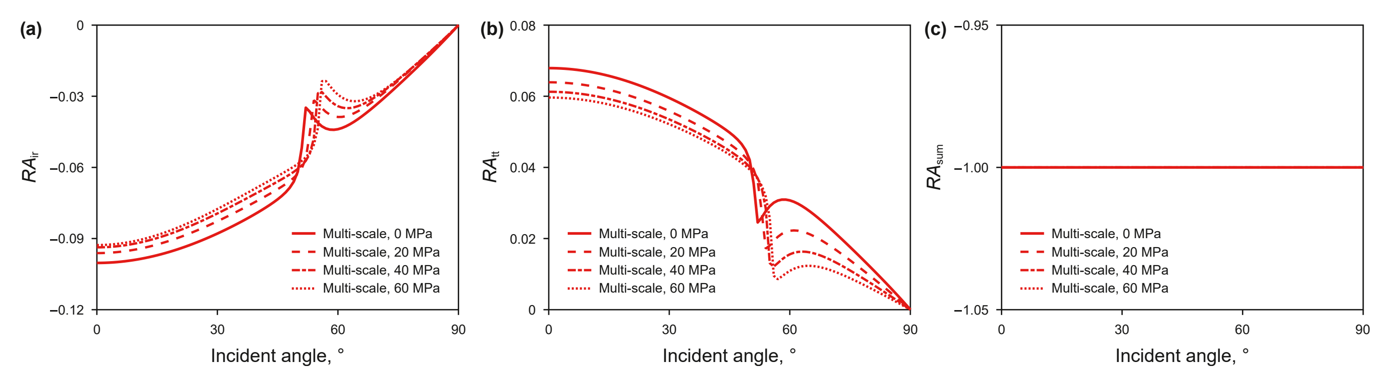

Fig. 11. Interference fluxes and energy-ratio sum as a function of incidence angle at 1 MHz and an inhomogeneity angle of 45°, under different effective stresses: (**a**) RA_{ir}, the interference contribution from incident–reflected and reflected wave interactions; (**b**) RA_{tt}, the contribution from transmitted waves; and (**c**) RA_{sum}, the sum of the energy ratios.

the increase in effective stress leads to a rise in the critical angle until it eventually stabilizes. Compared with the PAE model (Chen et al., 2024a), the slow P-wave R/T coefficients predicted by our new model are larger. This difference occurs because the proposed multiscale model further considers the attenuation induced by fluid patchy saturation, through which part of the fast P-wave energy is converted into slow P-wave energy at the patches (Carcione et al., 2003). Therefore, relative to the PAE model, the model proposed in this study is more applicable to investigating wave propagation and interface R/T in partially saturated media. Analysis of wave energy in Fig. 11 indicates that, as the effective stress increases, the absolute values of interference energy fluxes in both upper and lower spaces decrease. Despite variations in incident angle and effective stress, the total energy of the incident, reflected, and transmitted waves at the interface consistently satisfies the law of energy conservation.

Then, the R/T coefficients of the fast P-, slow P- and S-wave as a function of incidence angle at an effective stress of 0 MPa, under different frequencies and inhomogeneity angles, are also modeled, as shown in Fig. 12. The figure shows that the R/T coefficients for different inhomogeneity angles are quite similar at small incidence angles, but they become differentiated near the critical angle. Based on the previous analysis of wave dispersion (Fig. 4(c)), the slow P-wave velocity is very low at low frequencies but increases significantly at high frequencies. Consequently, the slow P-wave R/T coefficients at 1 MHz are much larger than those at 1 kHz and 5 Hz. In Fig. 13, the sum of all energy ratios equals −1, ensuring interface energy conservation under variations of frequency and inhomogeneity angle. Here, energy ratios are defined as the energy fluxes normalized by the incident energy flux, with the sign determined by the flux direction. Unlike the effect of effective stress, which influences interference energy fluxes across all

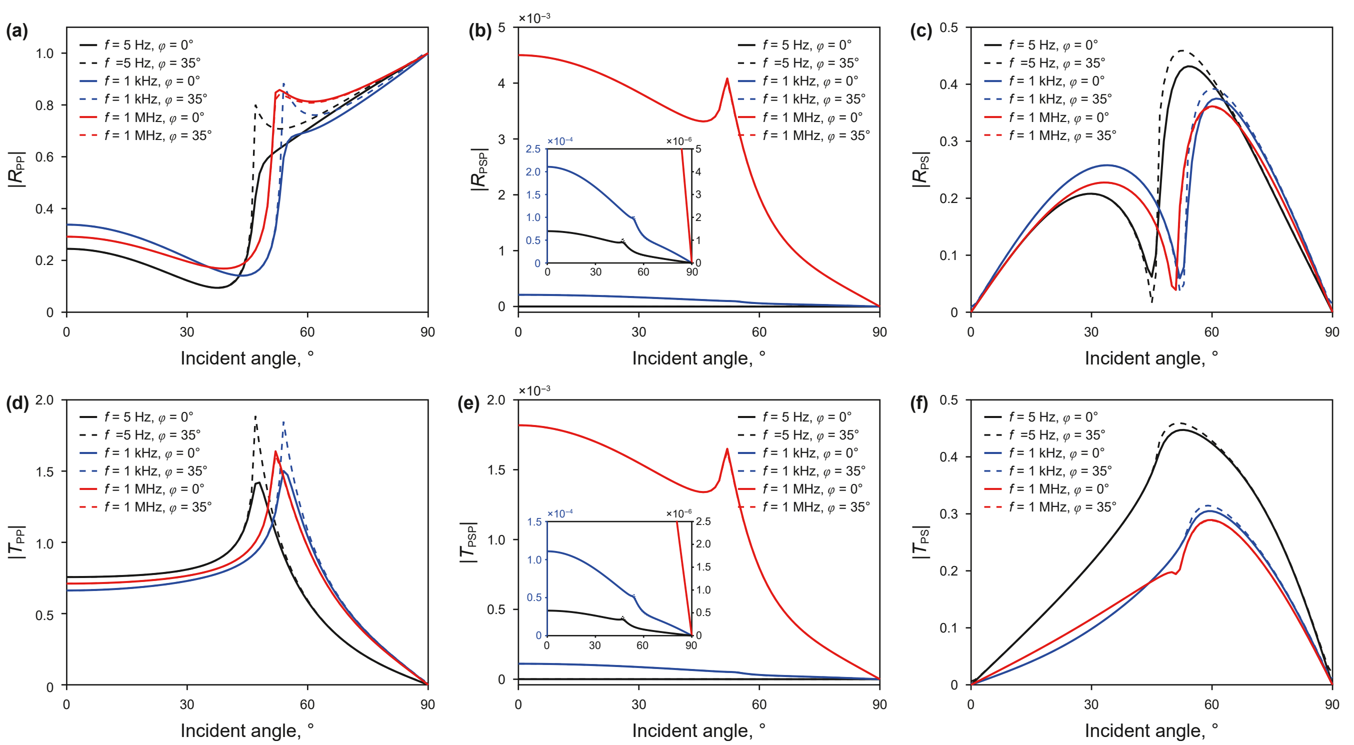

Fig. 12. R/T coefficients of fast P-wave **(a, d)**, slow P-wave **(b, e)** and S-wave **(c, f)** at the interface between two patchy-saturated porous media, as a function of incidence angle at an effective stress of 0 MPa, under different frequencies (5 Hz, 1 kHz and 1 MHz) and inhomogeneity angles (0° and 35°).

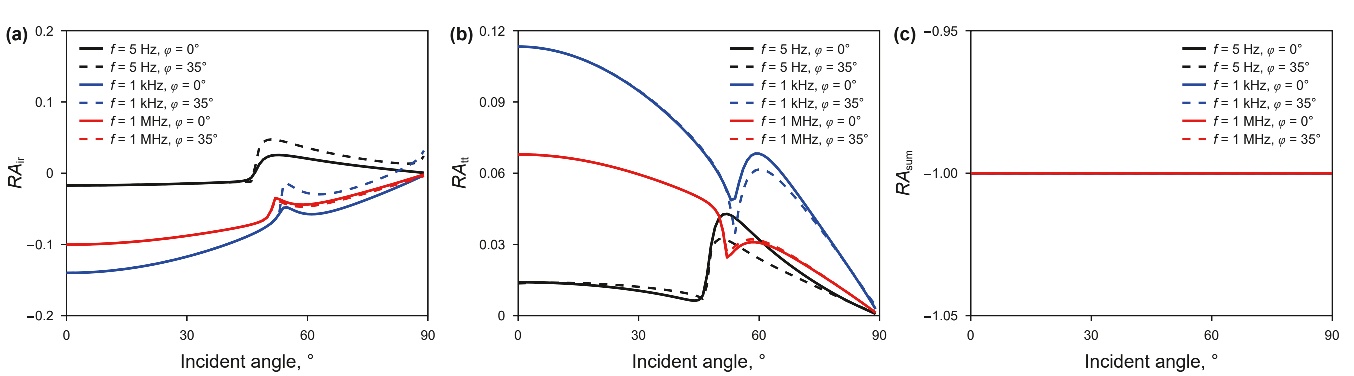

Fig. 13. Interference fluxes and energy-ratio sum as a function of incidence angle at 0 MPa, under different frequencies (5 Hz, 1 kHz and 1 MHz) and inhomogeneity angles (0° and 35°): **(a)** RA_{ir}, the interference contribution from incident–reflected and reflected wave interactions; **(b)** RA_{tt}, the contribution from transmitted waves; and **(c)** RA_{sum}, the sum of the energy ratios.

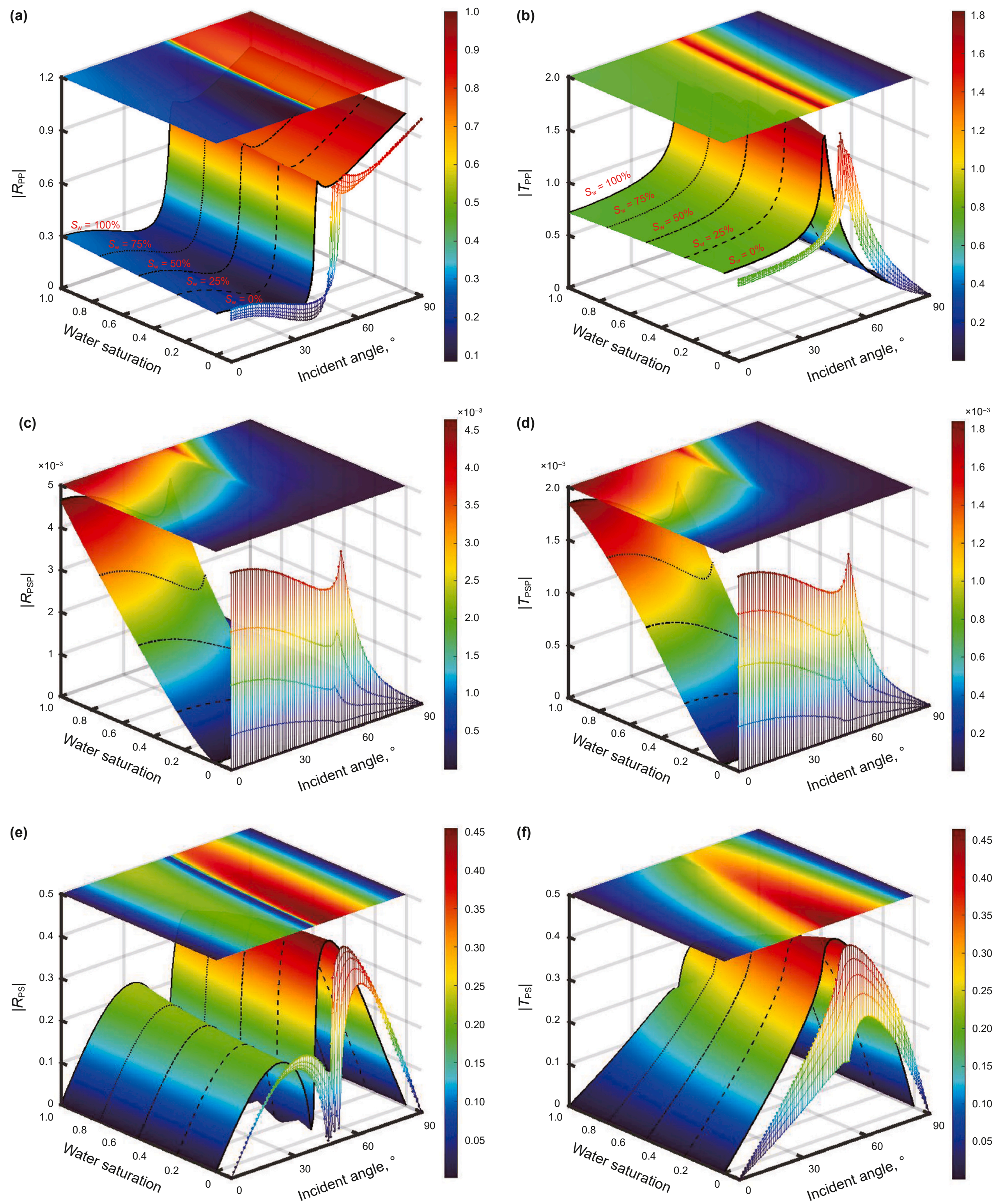

Fig. 14. R/T coefficients of fast P-wave **(a, b)**, slow P-wave **(c, d)** and S-wave **(e, f)** at the interface between two patchy-saturated porous media, as functions of incidence angle and water saturation S_w (frequency = 1 MHz, effective stress = 0 MPa and inhomogeneity angle = 45°). Curves extracted at water saturations of 0%, 25%, 50%, 75%, and 100% are shown for comparison.

incidence angles, the impact of inhomogeneity angle on interference energy fluxes are primarily observed at post-critical incidences.

Fig. 14 shows the variation of the R/T coefficients with water saturation, under the conditions of a frequency of 1 MHz, an effective stress of 0 MPa, and an inhomogeneity angle of 45°. At small incident angles, increasing water saturation leads to a rise in

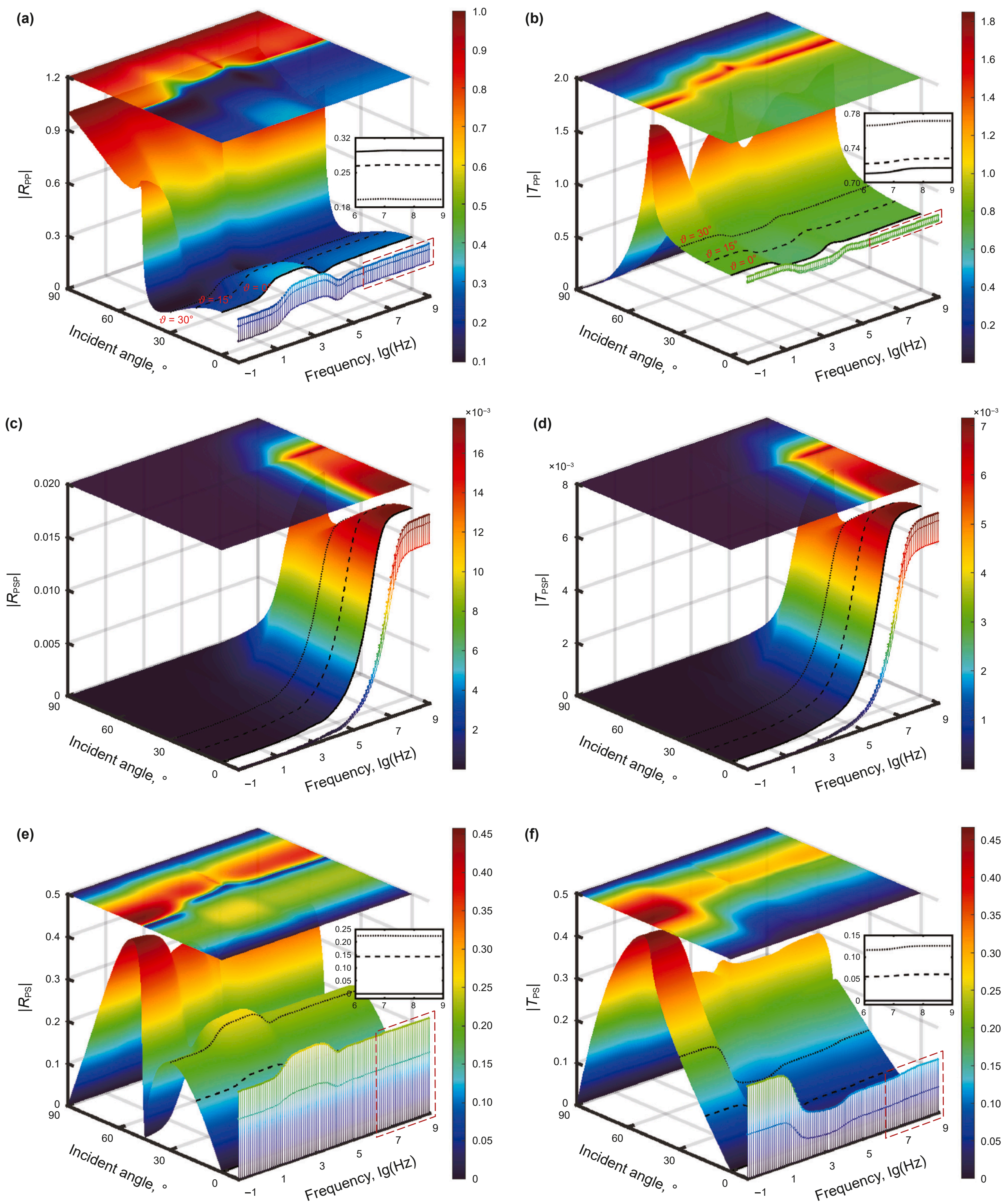

Fig. 15. R/T coefficients of fast P-wave (**a, b**), slow P-wave (**c, d**) and S-wave (**e, f**) at the interface between two patchy-saturated porous media, as functions of frequency and incidence angle ϑ (effective stress = 0 MPa and inhomogeneity angle = 0°). Curves extracted at incidence angles of 0°, 15°, and 30° are shown for comparison.

the amplitude of the fast P-wave reflection coefficient, while the transmission coefficient amplitude decreases, and the critical angles of both P- and S-waves increase. Moreover, the increase in water saturation enhances the energy of slow P-wave, which is consistent with the variation of slow P-wave velocity with water saturation shown in Fig. 5(b). In Fig. 15, we further investigate the variation of the R/T coefficients with frequency under the effective stress of 0 MPa and the inhomogeneity angle of 0°. It can be seen from the figure that the wave R/T characteristics exhibit significant frequency dependence. Considering that the incidence angle in practical seismic exploration is typically less than 40° (Wang et al., 2022), three angles (0°, 15°, and 30°) are selected for analysis. When the incidence angle is 0°, no S-wave is generated. As the incidence angle increases, the amplitude of the reflected fast P-wave decreases while its transmitted amplitude increases, the slow P-wave amplitude decreases and the S-wave amplitude increases. These trends are consistent with those shown in Figs. 10, 12 and 14. In addition, the pronounced frequency dependence of fast P- and S-wave R/T coefficients at 10^1–10^2 Hz and 10^4–10^5 Hz, respectively, corresponds to mesoscopic WIFF caused by patchy saturation and microscopic WIFF induced by squirt-flow interactions between stiff pores and cracks. Therefore, low-frequency dispersion should not be neglected in seismic interpretation. Meanwhile, a weaker frequency-dependent variation observed around 10^7 Hz is attributed to macroscopic global flow arising from the relative motion between the fluid and the rock skeleton.

To validate the proposed model, Fig. 16(b), (c) presents the comparison of R/T coefficients as a function of effective stress for a fast P-wave normally incident at the interface between the upper partially saturated tight sandstone sample B (see Table 2) and the lower medium I. Using wave velocities from the proposed model, the classical Liu model (Liu et al., 2021), and experimental measurements (He et al., 2024a; see Fig. 16(a)), the R/T coefficients are calculated according to the derived expressions in Eqs. (51) and (52). It can be observed from the figure that, under high effective stress, the R/T coefficients predicted by both our new model and classical Liu model agree well with the results calculated from measured velocities. However, when the effective stress is below approximately 30 MPa, the predictions of the classical Liu model deviate significantly from the R/T coefficients computed with laboratory velocities. In contrast, our proposed model indicates its applicability over a broader range of effective stress.

4. Discussion

The proposed stress- and frequency-dependent multiscale rock physics model is employed to derive exact R/T coefficient equations for an inhomogeneous wave obliquely incident on the interface between patchy-saturated porous media, and the associated R/T characteristics are subsequently analyzed. Considering that porosity does not always satisfy the assumption of being much less than 1, we propose a modified dual-porosity model to characterize the effect of effective stress on the pore structure. Compared with classical PAE theory, patchy saturation model, and squirt-flow model, our proposed model simultaneously accounts for effective stress as well as wave dispersion and attenuation over a broader frequency range (as shown in Table 3). Moreover, in contrast to the classical PAE theory (Chen et al., 2024a), our model provides an improved description of wave R/T behaviors in partially saturated porous media under stress, providing a theoretical and modeling basis for seismic exploration and fluid identification in complex reservoirs under in-situ stress conditions.

However, the present model is developed under the assumption that the material behavior remains within the elastic regime under in-situ stress. It does not explicitly account for irreversible deformation or damage of the rock and pore structure induced by engineering-relevant stress paths, such as dynamic disturbances

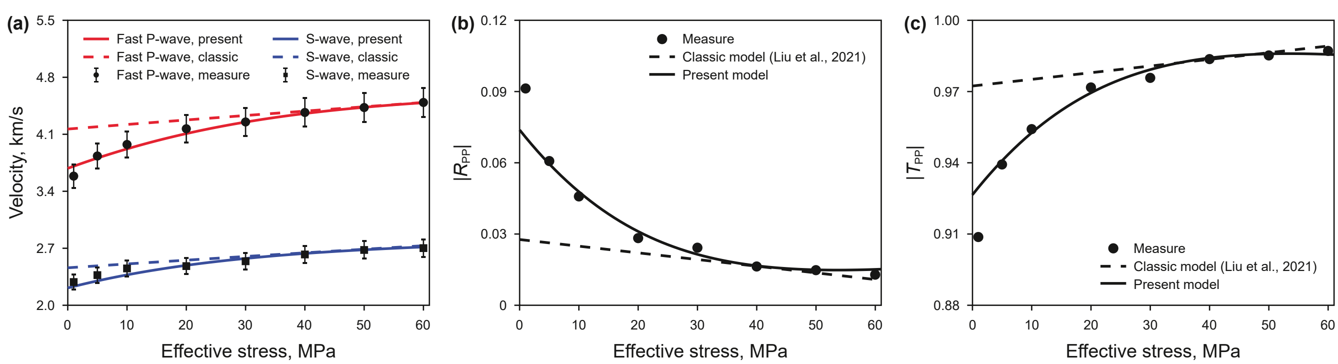

Fig. 16. Comparison of fast P- and S-wave velocities as functions of effective stress **(a)** predicted by our new model (solid lines), classical Liu's model (dashed lines) and experimental measurements (He et al., 2024a), as well as the corresponding R/T coefficients **(b, c)** of a fast P-wave at normal incidence at the interface between partially saturated tight sandstone B and Medium I. The error bars indicate ±4% errors.

Table 3
A comparison of the proposed model with several classical models.

Theory and model	WIFF mechanism	WIFF scale	Stress effect	Saturation heterogeneity
Biot (1956) poroelasticity theory	Wave-induced relative motion between pore fluid and solid	Macroscale	Neglected	Homogeneous
White (1975) patchy saturation model	Wave-induced pressure gradients between immiscible fluid patches	Mesoscale	Neglected	Patchy-saturated
Liu et al. (2021) PAE theory	Wave-induced relative motion between pore fluid and solid	Macroscale	Stress effect with 3oEC[a]	Homogeneous
Chen et al. (2024a) PAE theory	Wave-induced relative motion between pore fluid and solid	Macroscale	Stress effect with 3oEC[a] & cd[b]	Homogeneous
Chen et al. (2025) squirt-flow model	Wave-induced pressure gradients between pores and wedge-shape cracks	Microscale	Stress effect with cd[b]	Homogeneous
Present model	Integrated multiscale WIFF mechanism	Multiscale	Stress effect with 3oEC[a] & cd[b]	Patchy-saturated

[a] 3oEC = third-order elastic constants.
[b] cd = crack deformation.

or excavation. Consequently, the applicability of the model is primarily limited to in-situ states or the initial stages of engineering assessment. In addition, in our study, the boundary conditions are assumed to satisfy fluid pressure continuity. However, in real geotechnical-fluid interfaces (e.g., soil-water, rock-fluid contacts), factors like fluid viscosity, interfacial adsorption, and micro-scale heterogeneity may challenge the assumption of perfect fluid pressure continuity. In this case, further incorporating membrane stiffness into the fluid pressure boundary conditions is essential for accurately capturing the wave R/T behavior (Qi et al., 2021; Chen et al., 2024a). Furthermore, to analyze the cross-frequency effects of WIFF mechanisms at different scales on wave propagation, we sequentially incorporated the squirt-flow and patchy-saturation-induced WIFF mechanisms into the PAE theory. This approximate approach allows us to study wave dispersion, attenuation, and R/T characteristics in partially saturated porous media under in-situ stress. However, for certain crack aspect ratios and patchy scales, the squirt-flow and patchy-saturation mechanisms may operate within overlapping frequency bands, potentially leading to competition or partial screening effects. Therefore, investigating the coupling of these mechanisms to clarify their interaction represents an important direction for future research.

Moreover, our model assumes an isotropic medium and therefore cannot effectively account for velocity dispersion, attenuation, and R/T characteristics in anisotropic media. By incorporating layered structures or directionally aligned fractures into the modeling (Chen et al., 2023b; Guo and Gurevich, 2020a, 2020b; Zhao et al., 2019; Zong et al., 2025), the model can be extended to anisotropic cases. In addition, our model accounts only for in-situ effective stress (i.e., confining pressure minus pore pressure), whereas axial stresses that are also commonly present in the subsurface (e.g., uniaxial, biaxial, and triaxial stresses) are not included. Therefore, a further direction for development is to incorporate the influence of axial stresses on pore structure (Li et al., 2025; Pei et al., 2024), as well as the impact of stress-induced anisotropy on wave R/T coefficients (Chen et al., 2021; Liu et al., 2009). Such extensions can be implemented relatively easily based on our current model. Furthermore, heterogeneity within the solid skeleton can also induce mesoscopic WIFF (Ba et al., 2011; Wang et al., 2020; Zheng et al., 2017), which significantly affects wave velocities and R/T coefficients in the seismic frequency band. Therefore, investigating the R/T characteristics of double-porosity media under in-situ stress conditions represents another promising direction for future research. Besides in-situ stress, temperature has also been shown to significantly influence the elastic properties of deep rocks (Li et al., 2021). Therefore, incorporating temperature effects on wave propagation based on thermoporoelastic theory (Hou et al., 2023, 2024; Wang et al., 2021), and further developing coupled acoustothermoelastic model (Chen et al., 2022; Yang et al., 2025; Zong et al., 2023), offers a valuable avenue for further investigation.

5. Conclusions

In this study, we develop a stress- and frequency-dependent rock physics model to characterize the wave velocity dispersion and attenuation in patchy-saturated porous media under in situ effective stress, based on the PAE theory, patchy saturation model, wedge-shaped squirt-flow model, and dual-porosity theory. The model overcomes the limitations of classical PAE theory by incorporating nonlinear crack deformation effects while accounting for multiscale WIFF mechanisms. The results demonstrate that increasing effective stress promotes the closure of compliant cracks, leading to higher fast P-wave and S-wave velocities and reduced dispersion and attenuation. At high frequencies, the reduced stress sensitivity reflects the rock approaching an unrelaxed state. In contrast to the effect of effective stress, increasing water saturation enhances both velocity dispersion and attenuation. Modeling results indicate that the predicted fast P-wave dispersion and attenuation agree with single- and double-scale theories within their respective dominant frequency bands. Subsequently, exact expressions for the R/T coefficients of obliquely incident inhomogeneous plane waves are derived. It is found that variations in effective stress and water saturation induce significant changes in the R/T coefficients across all incident angles, whereas the effect of the inhomogeneity angle is mainly confined to the vicinity of the critical angle and becomes negligible at small incident angles. The critical angle increases with effective stress, while its stress sensitivity decreases at higher stress levels. The results further indicate that, as frequency increases, the R/T coefficients of fast P- and S-waves exhibit three dispersion characteristic frequencies, particularly pronounced within the seismic frequency range. Furthermore, compared with classical models, our predictions show improved agreement with experimental data, demonstrating the validity of the proposed framework over a broader range of frequencies and effective stresses. Our study and results provide a useful tool for seismic exploration of hydrocarbon reservoirs. The proposed framework may also be relevant to geotechnical earthquake engineering applications and dynamic monitoring of underground structures where fluid-solid interactions are significant.

CRediT authorship contribution statement

Jia-Yun Li: Writing – original draft, Visualization, Validation, Software, Methodology, Formal analysis, Data curation, Conceptualization. **Zhao-Yun Zong:** Writing – review & editing, Supervision, Resources, Project administration, Methodology, Investigation, Funding acquisition, Conceptualization. **Xing-Yao Yin:** Visualization, Resources, Funding acquisition, Formal analysis, Conceptualization. **Zhi-Wei Miao:** Validation, Resources, Funding acquisition, Data curation. **Shi-Kai Li:** Validation, Supervision, Resources, Investigation. **Wei Xiao:** Validation, Resources, Investigation, Data curation.

Declaration of competing interest

The authors declare that they have no known competing financial interests or personal relationships that could have appeared to influence the work reported in this paper.

Acknowledgments

The authors cordially thank the anonymous reviewers for their constructive suggestions that greatly improve the quality of our manuscript, and also thank the sponsorship of the National Natural Science Foundation of China (42430809, U24B2020), and the Key Technology for Geophysical Prediction of Ultra-Deep Carbonate Reservoirs (P24240). We also thank Fu-Bin Chen for his assistance in improving the quality of this article.

Appendix A. Modified fluid bulk modulus based on White's patchy-saturation model

White (1975) proposed a patchy saturation model, in which porous medium is divided into multiple areas, each consisting of two concentric spheres (Carcione et al., 2003). Assume that the inner sphere is gas-saturated with a radius of a, and the outer sphere is water-saturated with a radius of b. Accordingly, the gas saturation is given by $S_1 = a^3/b^3$, and the water saturation is given by $S_2 = 1 - a^3/b^3$.

By incorporating the porosity and modified frame moduli developed in this study, which accounts for effective stress and microscale squirt flow, into the mesoscopic patchy saturation model, the stress- and frequency-dependent expressions for the bulk and shear moduli of patchy-saturated porous media are obtained as follows:

$$K_{\mathrm{sat}}(p,\omega) = \frac{K_\infty(p,\omega)}{1 - K_\infty(p,\omega)W(p,\omega)} \tag{A.1}$$

$$\mu_{\mathrm{sat}}(p,\omega) = \frac{\mu_{\mathrm{mf}}^{(1)}(p,\omega)\mu_{\mathrm{mf}}^{(2)}(p,\omega)}{S_1\mu_{\mathrm{mf}}^{(2)}(p,\omega) + S_2\mu_{\mathrm{mf}}^{(1)}(p,\omega)} \tag{A.2}$$

with

$$W(p,\omega) = \frac{3ia\kappa(R_1 - R_2)}{b^3\omega\left(\eta^{(1)}Z_1 - \eta^{(2)}Z_2\right)}\left(\frac{K_{A1}}{K_1} - \frac{K_{A2}}{K_2}\right), \tag{A.3}$$

$$\alpha_j' = 1 - \frac{K_{\mathrm{mf}}^{(j)}(p,\omega)}{K_{\mathrm{gr}}}, \tag{A.11}$$

$$K_\infty = \frac{K_2\left[3K_1 + 4\mu_{\mathrm{mf}}^{(1)}(p,\omega)\right] + 4\left[\mu_{\mathrm{mf}}^{(1)}(p,\omega)K_1 - \mu_{\mathrm{mf}}^{(2)}(p,\omega)K_2\right]S_1}{\left[3K_1 + 4\mu_{\mathrm{mf}}^{(1)}(p,\omega)\right] - 3(K_1 - K_2)S_1}, \tag{A.12}$$

$$K_j = \frac{K_{\mathrm{gr}} - K_{\mathrm{mf}}^{(j)}(p,\omega) + \phi(p)K_{\mathrm{mf}}^{(j)}(p,\omega)\left(K_{\mathrm{gr}}\big/K_{fj} - 1\right)}{1 - \phi(p) - K_{\mathrm{mf}}^{(j)}(p,\omega)\big/K_{\mathrm{gr}} + \phi(p)K_{\mathrm{gr}}\big/K_{fj}}, j = 1,2. \tag{A.13}$$

where K_∞ represents the high-frequency bulk modulus in the absence of fluid flow between gas pockets. $K_j, j = 1,2$ refer to the low-frequency Gassmann moduli of gas-saturated and water-saturated rock, respectively.

Then, substituting the patchy-saturated rock bulk modulus K_{sat}, the modified frame moduli $K_{\mathrm{mf}}(p,\omega)$ and $\mu_{\mathrm{mf}}(p,\omega)$, and the stress-dependent porosity $\phi(p)$ into the Gassmann equation, the fluid bulk modulus accounting for mesoscopic WIFF is derived as

$$K_{\mathrm{f}}^{\#}(p,\omega) = \frac{\phi(p)\left[K_{\mathrm{sat}}(p,\omega) - K_{\mathrm{mf}}(p,\omega)\right]}{\left(1 - \frac{K_{\mathrm{mf}}(p,\omega)}{K_{\mathrm{gr}}}\right)^2 - \left[K_{\mathrm{sat}}(p,\omega) - K_{\mathrm{mf}}(p,\omega)\right]\left(\frac{1-\phi(p)}{K_{\mathrm{gr}}} - \frac{K_{\mathrm{mf}}(p,\omega)}{K_{\mathrm{gr}}^2}\right)} \tag{A.14}$$

$$R_1 = \frac{\left[K_1 - K_{\mathrm{mf}}^{(1)}(p,\omega)\right]\left[3K_2 + 4\mu_{\mathrm{mf}}^{(2)}(p,\omega)\right]}{K_2\left[3K_1 + 4\mu_{\mathrm{mf}}^{(1)}(p,\omega)\right] + 4\left[\mu_{\mathrm{mf}}^{(1)}(p,\omega)K_1 - \mu_{\mathrm{mf}}^{(2)}(p,\omega)K_2\right]S_1}, \tag{A.4}$$

$$R_2 = \frac{\left[K_2 - K_{\mathrm{mf}}^{(2)}(p,\omega)\right]\left[3K_1 + 4\mu_{\mathrm{mf}}^{(1)}(p,\omega)\right]}{K_2\left[3K_1 + 4\mu_{\mathrm{mf}}^{(1)}(p,\omega)\right] + 4\left[\mu_{\mathrm{mf}}^{(1)}(p,\omega)K_1 - \mu_{\mathrm{mf}}^{(2)}(p,\omega)K_2\right]S_1}, \tag{A.5}$$

$$Z_1 = \frac{1 - \exp(-2\chi_1 a)}{(\chi_1 a - 1) + (\chi_1 a + 1)\exp(-2\chi_1 a)}, \tag{A.6}$$

$$Z_2 = \frac{(\chi_2 b + 1) + (\chi_2 b - 1)\exp[2\chi_2(b-a)]}{(\chi_2 b + 1)(\chi_2 a - 1) - (\chi_2 b - 1)(\chi_2 a + 1)\exp[2\chi_2(b-a)]}, \tag{A.7}$$

$$\chi_j = \sqrt{i\omega\eta^{(j)}\big/\left(\kappa K_{Ej}\right)}, \tag{A.8}$$

$$K_{Ej} = \left[1 - \frac{\alpha_j' K_{fj}\left(1 - K_j\big/K_{\mathrm{gr}}\right)}{\phi(p)K_j\left(1 - K_{fj}\big/K_{\mathrm{gr}}\right)}\right]K_{Aj}, \tag{A.9}$$

$$K_{Aj} = \left[\frac{\phi(p)}{K_{fj}} + \frac{1}{K_{\mathrm{gr}}}\left[\alpha_j' - \phi(p)\right]\right]^{-1}, \tag{A.10}$$

Appendix B. Coefficients of dynamic equations

The generalized Lagrangian equation establishes a unified dynamic relationship among strain potential energy H, kinetic energy T, and dissipation energy D, given by

$$\frac{\mathrm{d}}{\mathrm{d}x_j}\frac{\partial H}{\partial u_{i,j}} = \frac{\mathrm{d}}{\mathrm{d}t}\left(\frac{\partial T}{\partial \dot{u}_i}\right) + \frac{\partial D}{\partial \dot{u}_i}, i,j = 1,2,3 \tag{B.1}$$

$$\frac{\mathrm{d}}{\mathrm{d}x_j}\frac{\partial H}{\partial w_{i,j}} = \frac{\mathrm{d}}{\mathrm{d}t}\left(\frac{\partial T}{\partial \dot{w}_i}\right) + \frac{\partial D}{\partial \dot{w}_i}, i,j = 1,2,3 \tag{B.2}$$

For the fluid-saturated porous medium, the kinetic energy T and dissipation energy D can be expressed as (Biot, 1956)

$$2T = \rho\dot{u}_i\dot{u}_i + 2\rho_{\mathrm{f}}\dot{u}_i\dot{w}_i + \rho_{\mathrm{m}}\dot{w}_i\dot{w}_i \tag{B.3}$$

$$2D = \frac{\eta}{\kappa}\dot{w}_i\dot{w}_i \tag{B.4}$$

where, $\rho_{\mathrm{m}} = \rho_{\mathrm{f}}\tau/\phi$, τ refers to the tortuosity of the pore space in the rock. η refers to the fluid viscosity. κ refers to the permeability of the rock.

Substituting Eqs. (16), (B.3) and (B.4) into the generalized Lagrangian Eqs. (B.1) and (B.2), and incorporating the "Small on Large" assumption, yields the dynamic equations (Liu et al., 2021; Chen et al., 2024a)

$$\rho\ddot{u}_i^d + \rho_{\mathrm{f}}\ddot{w}_i^d = \Theta_{ijkl}u_{k,lj}^d + \Gamma_{ij}w_{k,kj}^d \tag{B.5}$$

$$\rho_f \ddot{u}_i^d + \tilde{\rho}\ddot{w}_i^d = \Gamma_{kj} u_{k,ij}^d + \Gamma w_{k,ik}^d \tag{B.6}$$

with

$$\Gamma_{ij} = \alpha M\left(\delta_{ij} + u_{i,j}^s\right) + \gamma\left(u_{i,j}^s + u_{j,i}^s\right)\Big/2 - (2\gamma_2 + \gamma)\delta_{ij} u_{m,m}^s + (\alpha M + 2\gamma_3)\delta_{ij} w_{m,m}^s, \tag{B.7}$$

$$\Gamma_{kj} = \alpha M\left(\delta_{kj} + u_{k,j}^s\right) + \gamma\left(u_{k,j}^s + u_{j,k}^s\right)\Big/2 - (2\gamma_2 + \gamma)\delta_{kj} u_{m,m}^s + (\alpha M + 2\gamma_3)\delta_{kj} w_{m,m}^s, \tag{B.8}$$

$$\Gamma = M + (2\gamma_3 + \alpha M) u_{m,m}^s - 3(M - 2\gamma_1) w_{m,m}^s, \tag{B.9}$$

$$\Theta_{ijkl} = \left(a_{ijkl} + \alpha^2 M \delta_{ij}\delta_{kl}\right) + b_{ijklmn} u_{m,n}^s + b_{ijkl} w_{m,m}^s. \tag{B.10}$$

and

$$a_{ijkl} = \left(\lambda_u - \alpha^2 M\right)\delta_{ij}\delta_{kl} + \mu_d \delta_{ik}\delta_{jl} + \mu_d \delta_{jk}\delta_{il}, \tag{B.11}$$

$$\begin{aligned} b_{ijklmn} = {} & c_{ijklmn} + \lambda_u\left(\delta_{ij}\delta_{nl}\delta_{mk} + \delta_{ik}\delta_{jl}\delta_{mn} + \delta_{im}\delta_{jn}\delta_{kl}\right) \\ & + \mu_d\left(\delta_{jl}\delta_{in}\delta_{mk} + \delta_{il}\delta_{jn}\delta_{mk} + \delta_{ik}\delta_{ml}\delta_{jn} + \delta_{im}\delta_{jl}\delta_{kn} + \delta_{ik}\delta_{nl}\delta_{jm} + \delta_{im}\delta_{jk}\delta_{nl}\right), \end{aligned} \tag{B.12}$$

$$b_{ijkl} = (\alpha M + \gamma/2)\delta_{ik}\delta_{jl} - 2(\gamma_2 + \gamma/2)\delta_{ij}\delta_{kl} + \gamma\delta_{jk}\delta_{il}\Big/2, \tag{B.13}$$

$$\begin{aligned} c_{ijklmn} = {} & \nu_1' \delta_{ij}\delta_{kl}\delta_{mn} + 2\nu_2'\left(\delta_{ij} d_{klmn} + \delta_{kl} d_{mnij} + \delta_{mn} d_{ijkl}\right) \\ & + 2\nu_3'\left(\delta_{ik} d_{jlmn} + \delta_{il} d_{jkmn} + \delta_{jk} d_{ilmn} + \delta_{jl} d_{ikmn}\right), \end{aligned} \tag{B.14}$$

$$d_{ijkl} = \left(\delta_{ik}\delta_{jl} + \delta_{il}\delta_{jk}\right)\Big/2. \tag{B.15}$$

where $\mathbf{u}^s$ and $\mathbf{w}^s$ represent the displacement of solid and relative fluid induced by stress, respectively. δ_{ij} refers to the Kronecker delta function.

Appendix C. Constitutive relationship in patchy-saturated porous media considering the effect of WIFF and effective stress

Based on the strain potential energy provided in Eq. (16), the solid and fluid stress components of the patchy-saturated porous medium with the effect of in-situ stress are given by (Chen et al., 2024a)

$$\sigma_{ij} = \frac{\partial H}{\partial E_{ij}} = \Upsilon_{ij}\frac{\partial u_i}{\partial x_i} + \Lambda\left(\frac{\partial u_i}{\partial x_j} + \frac{\partial u_j}{\partial x_i}\right) + \Gamma_{ij}\frac{\partial w_i}{\partial x_i} \tag{C.1}$$

$$p_f = \frac{\partial H}{\partial \zeta} = \tilde{\Upsilon}\frac{\partial u_i}{\partial x_i} + \tilde{\Lambda}_{ij}\frac{\partial u_i}{\partial x_j} + \tilde{\Gamma}\frac{\partial w_i}{\partial x_i} \tag{C.2}$$

with

$$\begin{cases} \Upsilon_{ij} = (1 + e^s)(\lambda_u + 2\gamma_2\zeta^s + \gamma\zeta^s)\delta_{ij} + \nu_1' e^s \delta_{ij}, \\ \Lambda = \mu_d - \dfrac{1}{2}\left[\gamma\zeta^s - (2\mu_d - \gamma\zeta^s + 6\nu_2' + 8\nu_3')e^s\right], \\ \Gamma_{ij} = (2\gamma_2 + \gamma)e^s\delta_{ij} - \gamma e_{ij}^s + 2\gamma_3\zeta^s\delta_{ij} - \alpha M\delta_{ij}. \end{cases} \tag{C.3}$$

$$\begin{cases} \tilde{\Upsilon} = -\alpha M + 2\gamma_3\zeta^s + (2\gamma_2 + \gamma)e^s, \\ \tilde{\Lambda}_{ij} = -\gamma e_{ij}^s, \\ \tilde{\Gamma} = M + 6\gamma_1\zeta^s + 2\gamma_3 e^s. \end{cases} \tag{C.4}$$

where $\lambda_u = \lambda_{mf}(p,\omega) + \alpha^2 M$, $\mu_d = \mu_{mf}(p,\omega)$, $\alpha = 1 - K_{mf}(p,\omega)/K_{gr}$ and $M = \left[(\alpha - \phi(p))/K_{gr} + \phi(p)/K_f^{\#}(p,\omega)\right]^{-1}$ represent four 2oECs that couple the effects of mesoscale and microscale WIFF.

Appendix D. Detailed expressions for the wave R/T coefficients

A sixth-order linear system, formulated in terms of the solid displacement potential amplitude ratios of the reflected and transmitted waves relative to the incident wave, is derived as follows:

$$\mathbf{Gx} = \mathbf{B} \tag{D.1}$$

with

$$G_{11}=s_1^{(\mathrm{I})},G_{12}=s_1^{(\mathrm{I})},G_{13}=-s_3^{(\mathrm{S1})},G_{14}=-s_1^{(\mathrm{I})},G_{15}=-s_1^{(\mathrm{I})},G_{16}=s_3^{(\mathrm{S2})}. \tag{D.2}$$

$$G_{21}=s_3^{(\mathrm{P1})},G_{22}=s_3^{(\mathrm{SP1})},G_{23}=s_1^{(\mathrm{I})},G_{24}=-s_3^{(\mathrm{P2})},G_{25}=-s_3^{(\mathrm{SP2})},G_{26}=-s_1^{(\mathrm{I})}. \tag{D.3}$$

$$\begin{aligned}
G_{31}&=\Upsilon_{33}^{(1)}\left(s_1^{(\mathrm{I})}\right)^2+\left(\Upsilon_{33}^{(1)}+2\Lambda^{(1)}\right)\left(s_3^{(\mathrm{P1})}\right)^2,\\
G_{32}&=\left(\Upsilon_{33}^{(1)}+\Gamma_{33}^{(1)}\xi^{(1)}\right)\left(s_1^{(\mathrm{I})}\right)^2+\left(\Upsilon_{33}^{(1)}+2\Lambda^{(1)}+\Gamma_{33}^{(1)}\xi^{(1)}\right)\left(s_3^{(\mathrm{SP1})}\right)^2,\\
G_{33}&=2\Lambda^{(1)}s_1^{(\mathrm{I})}s_3^{(\mathrm{S1})},\\
G_{34}&=-\Upsilon_{33}^{(2)}\left(s_1^{(\mathrm{I})}\right)^2-\left(\Upsilon_{33}^{(2)}+2\Lambda^{(2)}\right)\left(s_3^{(\mathrm{P2})}\right)^2,\\
G_{35}&=-\left(\Upsilon_{33}^{(2)}+\Gamma_{33}^{(2)}\xi^{(2)}\right)\left(s_1^{(\mathrm{I})}\right)^2-\left(\Upsilon_{33}^{(2)}+2\Lambda^{(2)}+\Gamma_{33}^{(2)}\xi^{(2)}\right)\left(s_3^{(\mathrm{SP2})}\right)^2,\\
G_{36}&=-2\Lambda^{(2)}s_1^{(\mathrm{I})}s_3^{(\mathrm{S2})}.
\end{aligned} \tag{D.4}$$

$$\begin{aligned}
G_{41}&=2\Lambda^{(1)}s_1^{(\mathrm{I})}s_3^{(\mathrm{P1})},G_{42}=2\Lambda^{(1)}s_1^{(\mathrm{I})}s_3^{(\mathrm{SP1})}+\Gamma_{13}^{(1)}\xi^{(1)}\left(s_1^{(\mathrm{I})}\right)^2+\Gamma_{13}^{(1)}\xi^{(1)}\left(s_3^{(\mathrm{SP1})}\right)^2,\\
G_{43}&=\Lambda^{(1)}\left(s_1^{(\mathrm{I})}\right)^2-\Lambda^{(1)}\left(s_3^{(\mathrm{S1})}\right)^2,G_{44}=-2\Lambda^{(2)}s_1^{(\mathrm{I})}s_3^{(\mathrm{P2})},\\
G_{45}&=-2\Lambda^{(2)}s_1^{(\mathrm{I})}s_3^{(\mathrm{SP2})}-\Gamma_{13}^{(2)}\xi^{(2)}\left(s_1^{(\mathrm{I})}\right)^2-\Gamma_{13}^{(2)}\xi^{(2)}\left(s_3^{(\mathrm{SP2})}\right)^2,\\
G_{46}&=-\Lambda^{(2)}\left(s_1^{(\mathrm{I})}\right)^2+\Lambda^{(2)}\left(s_3^{(\mathrm{S2})}\right)^2.
\end{aligned} \tag{D.5}$$

$$G_{51}=0,G_{52}=\xi^{(1)}s_3^{(\mathrm{SP1})},G_{53}=0,G_{54}=0,G_{55}=-\xi^{(2)}s_3^{(\mathrm{SP2})},G_{56}=0. \tag{D.6}$$

$$\begin{aligned}
G_{61}&=\tilde{\Upsilon}^{(1)}\left[\left(s_1^{(\mathrm{I})}\right)^2+\left(s_3^{(\mathrm{P1})}\right)^2\right]+\tilde{\Lambda}_{11}^{(1)}\left(s_1^{(\mathrm{I})}\right)^2+2\tilde{\Lambda}_{13}^{(1)}s_1^{(\mathrm{I})}s_3^{(\mathrm{P1})}+\tilde{\Lambda}_{33}^{(1)}\left(s_3^{(\mathrm{P1})}\right)^2,\\
G_{62}&=\tilde{\Upsilon}^{(1)}\left[\left(s_1^{(\mathrm{I})}\right)^2+\left(s_3^{(\mathrm{SP1})}\right)^2\right]+\tilde{\Lambda}_{11}^{(1)}\left(s_1^{(\mathrm{I})}\right)^2+2\tilde{\Lambda}_{13}^{(1)}s_1^{(\mathrm{I})}s_3^{(\mathrm{SP1})}+\tilde{\Lambda}_{33}^{(1)}\left(s_3^{(\mathrm{SP1})}\right)^2+\tilde{\Gamma}^{(1)}\xi^{(1)}\left[\left(s_1^{(\mathrm{I})}\right)^2+\left(s_3^{(\mathrm{SP1})}\right)^2\right],\\
G_{63}&=-\tilde{\Lambda}_{11}^{(1)}s_1^{(\mathrm{I})}s_3^{(\mathrm{S1})}+\tilde{\Lambda}_{13}^{(1)}\left(s_1^{(\mathrm{I})}\right)^2-\tilde{\Lambda}_{13}^{(1)}\left(s_3^{(\mathrm{S1})}\right)^2+\tilde{\Lambda}_{33}^{(1)}s_1^{(\mathrm{I})}s_3^{(\mathrm{S1})},\\
G_{64}&=-\tilde{\Upsilon}^{(2)}\left[\left(s_1^{(\mathrm{I})}\right)^2+\left(s_3^{(\mathrm{P2})}\right)^2\right]-\tilde{\Lambda}_{11}^{(2)}\left(s_1^{(\mathrm{I})}\right)^2-2\tilde{\Lambda}_{13}^{(2)}s_1^{(\mathrm{I})}s_3^{(\mathrm{P2})}-\tilde{\Lambda}_{33}^{(2)}\left(s_3^{(\mathrm{P2})}\right)^2,\\
G_{65}&=-\tilde{\Upsilon}^{(2)}\left[\left(s_1^{(\mathrm{I})}\right)^2+\left(s_3^{(\mathrm{SP2})}\right)^2\right]-\tilde{\Lambda}_{11}^{(2)}\left(s_1^{(\mathrm{I})}\right)^2-2\tilde{\Lambda}_{13}^{(2)}s_1^{(\mathrm{I})}s_3^{(\mathrm{SP2})}-\tilde{\Lambda}_{33}^{(2)}\left(s_3^{(\mathrm{SP2})}\right)^2-\tilde{\Gamma}^{(2)}\xi^{(2)}\left[\left(s_1^{(\mathrm{I})}\right)^2+\left(s_3^{(\mathrm{SP2})}\right)^2\right],\\
G_{66}&=\tilde{\Lambda}_{11}^{(2)}s_1^{(\mathrm{I})}s_3^{(\mathrm{S2})}-\tilde{\Lambda}_{13}^{(2)}\left(s_1^{(\mathrm{I})}\right)^2+\tilde{\Lambda}_{13}^{(2)}\left(s_3^{(\mathrm{S2})}\right)^2-\tilde{\Lambda}_{33}^{(2)}s_1^{(\mathrm{I})}s_3^{(\mathrm{S2})}.
\end{aligned} \tag{D.7}$$

and

$$\begin{aligned}
b_1&=-s_1^{(\mathrm{I})}\Re+(1-\Re)s_3^{(\mathrm{I})},\\
b_2&=-s_3^{(\mathrm{I})}\Re-(1-\Re)s_1^{(\mathrm{I})},\\
b_3&=-\Re\left[\Upsilon_{33}^{(1)}\left(s_1^{(\mathrm{I})}\right)^2+\left(\Upsilon_{33}^{(1)}+2\Lambda^{(1)}\right)\left(s_3^{(\mathrm{I})}\right)^2\right]-2(1-\Re)\Lambda^{(1)}s_1^{(\mathrm{I})}s_3^{(\mathrm{I})},\\
b_4&=-2\Re\Lambda^{(1)}s_1^{(\mathrm{I})}s_3^{(\mathrm{I})}-(1-\Re)\Lambda^{(1)}\left[\left(s_1^{(\mathrm{I})}\right)^2-\left(s_3^{(\mathrm{I})}\right)^2\right],\\
b_5&=0,\\
b_6&=-\Re\left[\tilde{\Upsilon}^{(1)}\left(s_1^{(\mathrm{I})}\right)^2+\tilde{\Upsilon}^{(1)}\left(s_3^{(\mathrm{I})}\right)^2+\tilde{\Lambda}_{11}^{(1)}\left(s_1^{(\mathrm{I})}\right)^2+2\tilde{\Lambda}_{13}^{(1)}s_1^{(\mathrm{I})}s_3^{(\mathrm{I})}+\tilde{\Lambda}_{33}^{(1)}\left(s_3^{(\mathrm{I})}\right)^2\right]-(1-\Re)\left[\tilde{\Lambda}_{13}^{(1)}\left(s_1^{(\mathrm{I})}\right)^2-\tilde{\Lambda}_{13}^{(1)}\left(s_3^{(\mathrm{I})}\right)^2-\tilde{\Lambda}_{11}^{(1)}s_1^{(\mathrm{I})}s_3^{(\mathrm{I})}+\tilde{\Lambda}_{33}^{(1)}s_1^{(\mathrm{I})}s_3^{(\mathrm{I})}\right].
\end{aligned} \tag{D.8}$$

By substituting Eqs. (D.2)–(D.8) into Eq. (D.1), the reflection and transmission coefficients are expressed in terms of the complex amplitude ratios of the solid displacement potential.

References

Alkhimenkov, Y., Quintal, B., 2024. A simple and accurate model for attenuation and dispersion caused by squirt flow in isotropic porous rocks. Geophysics 89 (1), MR1–MR10. https://doi.org/10.1190/geo2023-0049.1.

Ba, J., Carcione, J.M., Cao, H., et al., 2013. Poro-acoustoelasticity of fluid-saturated rocks. Geophys. Prospect. 61 (3), 599–612. https://doi.org/10.1111/j.1365-2478.2012.01091.x.

Ba, J., Carcione, J.M., Nie, J.X., 2011. Biot-rayleigh theory of wave propagation in double-porosity media. J. Geophys. Res. Solid Earth 116 (B6), B06202. https://doi.org/10.1029/2010JB008185.

Ba, J., Ma, R., Carcione, J.M., et al., 2023. Effects of pore geometry and saturation on the behavior of multiscale waves in tight sandstone layers. J. Geophys. Res. Solid Earth 128 (12), e2023JB027542. https://doi.org/10.1029/2023JB027542.

Ba, J., Wei, Y., Carcione, J.M., et al., 2024. Stress and frequency dependence of wave velocities in saturated rocks based on acoustoelasticity with squirt-flow dissipation. Geophys. J. Int. 236 (3), 1753–1763. https://doi.org/10.1093/gji/ggae020.

Ba, J., Xu, W., Fu, L.Y., et al., 2017. Rock anelasticity due to patchy saturation and fabric heterogeneity: A double double-porosity model of wave propagation. J. Geophys. Res. Solid Earth 122 (3), 1949–1976. https://doi.org/10.1002/2016JB013882.

Biot, M.A., 1956. Theory of propagation of elastic waves in a fluid-saturated porous solid. I. Low-frequency range. J. Acoust. Soc. Am. 28 (2), 168–178. https://doi.org/10.1121/1.1908239.

Biot, M.A., 1962. Mechanics of deformation and acoustic propagation in porous media. J. Appl. Phys. 33 (4), 1482–1498. https://doi.org/10.1063/1.1728759.

Biot, M.A., 1972. Theory of finite deformations of porous solids. Ind. Univ. Math. J. 21 (7), 597–620. https://www.jstor.org/stable/24890361.

Biot, M.A., 1973. Nonlinear and semilinear rheology of porous solids. J. Geophys. Res. 78 (23), 4924–4937. https://doi.org/10.1029/JB078i023p04924.

Carcione, J.M., Helle, H.B., Pham, N.H., 2003. White's model for wave propagation in partially saturated rocks: Comparison with poroelastic numerical experiments. Geophysics 68 (4), 1389–1398. https://doi.org/10.1190/1.1598132.

Chen, F., Zong, Z., Jiang, M., 2021. Seismic reflectivity and transmissivity parametrization with the effect of normal in situ stress. Geophys. J. Int. 226 (3), 1599–1614. https://doi.org/10.1093/gji/ggab179.

Chen, F., Zong, Z., Rezaee, R., et al., 2024a. Pressure effects on plane wave reflection and transmission in fluid-saturated porous media. Surv. Geophys. 45 (4), 1245–1290. https://doi.org/10.1007/s10712-024-09829-9.

Chen, F., Zong, Z., Yin, X., 2022. Acoustothermoelasticity for joint effects of stress and thermal fields on wave dispersion and attenuation. J. Geophys. Res. Solid Earth 127 (4), e2021JB023671. https://doi.org/10.1029/2021JB023671.

Chen, F., Zong, Z., Yin, X., 2023a. Monitoring the change in horizontal stress with multi-wave time-lapse seismic response based on nonlinear elasticity theory. Pet. Sci. 20 (2), 815–826. https://doi.org/10.1016/j.petsci.2022.09.022.

Chen, F., Zong, Z., Yin, X., 2024b. Research progress on seismic reflection and transmission based on solid acoustoelasticity theory. Rev. Geophys. Planet Phys. 55 (3), 344–357. https://doi.org/10.19975/j.dqyxx.2023-023.

Chen, F., Zong, Z., Yin, X., 2025. A squirt-flow model in isotropic porous rocks containing wedge-shaped cracks and its interpretation for laboratory measurements. Geophysics 90 (2), MR141–MR153. https://doi.org/10.1190/geo2024-0292.1.

Chen, F., Zong, Z., Yin, X., et al., 2023b. Stress dependence of elastic wave dispersion and attenuation in fluid-saturated porous layered media. Sci. China Earth Sci. 66 (11), 2622–2634. https://doi.org/10.1007/s11430-022-1147-7.

David, E.C., Zimmerman, R.W., 2012. Pore structure model for elastic wave velocities in fluid-saturated sandstones. J. Geophys. Res. Solid Earth 117 (B7), B07210. https://doi.org/10.1029/2012JB009195.

Denneman, A.I., Drijkoningen, G.G., Smeulders, D.M., et al., 2002. Reflection and transmission of waves at a fluid/porous-medium interface. Geophysics 67 (1), 282–291. https://doi.org/10.1190/1.1451800.

Detournay, E., Cheng, H.D., 1993. Fundamentals of poroelasticity. Anal. Des. Methods 140 (1), 113–171. https://doi.org/10.1016/B978-0-08-040615-2.50011-3.

Dutta, N.C., Odé, H., 1979a. Attenuation and dispersion of compressional waves in fluid-filled porous rocks with partial gas saturation (white model); part I, biot theory. Geophysics 44 (11), 1777–1788. https://doi.org/10.1190/1.1440938.

Dutta, N.C., Odé, H., 1979b. Attenuation and dispersion of compressional waves in fluid-filled porous rocks with partial gas saturation (white model); part II, results. Geophysics 44 (11), 1789–1805. https://doi.org/10.1190/1.1440939.

Dutta, N.C., Odé, H., 1983. Seismic reflections from a gas-water contact. Geophysics 48 (2), 148–162. https://doi.org/10.1190/1.1441454.

Dutta, N.C., Seriff, A.J., 1979. On White's model of attenuation in rocks with partial gas saturation. Geophysics 44 (11), 1806–1812. https://doi.org/10.1190/1.1440940.

Fagbemi, S., Tahmasebi, P., Piri, M., 2018. Pore-scale modeling of multiphase flow through porous media under triaxial stress. Adv. Water Resour. 122, 206–216. https://doi.org/10.1016/j.advwatres.2018.10.018.

Fagbemi, S., Tahmasebi, P., Piri, M., 2020. Numerical modeling of strongly coupled microscale multiphase flow and solid deformation. Int. J. Numer. Anal. Model. 44 (2), 161–182. https://doi.org/10.1002/nag.2999.

Fu, B.Y., Fu, L.Y., 2018. Poro-acoustoelasticity with compliant pores for fluid-saturated rocks. Geophysics 83 (3), WC1–WC14. https://doi.org/10.1190/geo2017-0423.1.

Geertsma, J., Smit, D.C., 1961. Some aspects of elastic wave propagation in fluid-saturated porous solids. Geophysics 26 (2), 169–181. https://doi.org/10.1190/1.1438855.

Guo, J., Gurevich, B., 2020a. Effects of coupling between wave-induced fluid flow and elastic scattering on p-wave dispersion and attenuation in rocks with aligned fractures. J. Geophys. Res. Solid Earth 125 (3), e2019JB018685. https://doi.org/10.1029/2019JB018685.

Guo, J., Gurevich, B., 2020b. Frequency-dependent P wave anisotropy due to wave-induced fluid flow and elastic scattering in a fluid-saturated porous medium with aligned fractures. J. Geophys. Res. Solid Earth 125 (8), e2020JB020320. https://doi.org/10.1029/2020JB020320.

Gurevich, B., Ciz, R., Denneman, A.I., 2004. Simple expressions for normal-incidence reflection coefficients from an interface between fluid-saturated porous materials. Geophysics 69 (6), 1372–1377. https://doi.org/10.1190/1.1836811.

Gurevich, B., Makarynska, D., de Paula, O.B., et al., 2010. A simple model for squirt-flow dispersion and attenuation in fluid-saturated granular rocks. Geophysics 75 (6), N109–N120. https://doi.org/10.1190/1.3509782.

He, Y.X., Wang, S., Li, H., et al., 2024a. Laboratory experiments and theoretical study of pressure and fluid influences on acoustic response in tight rocks with pore microstructure. Geophys. Prospect. 72 (5), 1896–1918. https://doi.org/10.1111/1365-2478.13466.

He, Y.X., Wang, S., Tang, G., et al., 2024b. A seismic elastic moduli module for the measurements of low-frequency wave dispersion and attenuation of fluid-saturated rocks under different pressures. Pet. Sci. 21 (1), 162–181. https://doi.org/10.1016/j.petsci.2023.08.036.

Hill, R., 1952. The elastic behaviour of a crystalline aggregate. Proc. Phys. Soc. 65 (5), 349–354. https://doi.org/10.1088/0370-1298/65/5/307.

Hou, W., Fu, L.Y., Carcione, J.M., 2022. Reflection and transmission of thermoelastic waves in multilayered media. Geophysics 87 (3), MR117–MR128. https://doi.org/10.1190/geo2021-0542.1.

Hou, W., Fu, L.Y., Carcione, J.M., 2023. Reflection and transmission of inhomogeneous plane waves in thermoporoelastic media. Surv. Geophys. 44 (6), 1897–1917. https://doi.org/10.1007/s10712-023-09782-z.

Hou, W., Fu, L.Y., Carcione, J.M., 2024. Reflection, transmission, and AVO response of inhomogeneous plane waves in thermoporoelastic media with two-temperature equations of heat conduction. Geophysics 89 (5), MR297–MR307. https://doi.org/10.1190/geo2023-0625.1.

Jiang, S., Wei, W., Cai, J., 2025. Seismic wave propagation in partially saturated fractal porous media. Geophysics 90 (2), MR113–MR128. https://doi.org/10.1190/geo2024-0028.1.

Johnson, D.L., 2001. Theory of frequency dependent acoustics in patchy-saturated porous media. J. Acoust. Soc. Am. 110 (2), 682–694. https://doi.org/10.1121/1.1381021.

Kumar, M., Kumari, M., Barak, M.S., 2018. Reflection of plane seismic waves at the surface of double-porosity dual-permeability materials. Pet. Sci. 15 (3), 521–537. https://doi.org/10.1007/s12182-018-0245-y.

Kumari, M., Barak, M.S., Kumar, M., 2017. Seismic reflection and transmission coefficients of a single layer sandwiched between two dissimilar poroelastic solids. Pet. Sci. 14, 676–693. https://doi.org/10.1007/s12182-017-0195-9.

Kumari, M., Kaswan, P., Kumar, M., et al., 2025. Seismic wave reflection characteristics and wave-induced fluid flow in unsaturated porous solid. Sci. Rep. 15 (1), 18840. https://doi.org/10.1038/s41598-025-97275-x.

Levenberg, K., 1944. A method for the solution of certain non-linear problems in least squares. Q. Appl. Math. 2 (2), 164–168. https://www.jstor.org/stable/43633451.

Li, J., Zong, Z., Chen, F., 2025. A dual-porosity model incorporating uniaxial stress effect and its application in wave velocity estimation with well-logging data. Geophys. Prospect. 73 (2), 712–731. https://doi.org/10.1111/1365-2478.13620.

Li, N., Fu, L.Y., Yang, J., et al., 2021. On three-stage temperature dependence of elastic wave velocities for rocks. J. Geophys. Eng. 18 (3), 328–338. https://doi.org/10.1093/jge/gxab017.

Ling, W., Ba, J., Carcione, J.M., et al., 2021. Poroacoustoelasticity for rocks with a dual-pore structure. Geophysics 86 (1), MR17–MR25. https://doi.org/10.1190/geo2020-0314.1.

Liu, J., Cui, Z., Sevostianov, I., 2021. Effect of stresses on wave propagation in fluid-saturated porous media. Int. J. Eng. Sci. 167, 103519. https://doi.org/10.1016/j.ijengsci.2021.103519.

Liu, J., Cui, Z., Wang, K., 2009. The relationships between uniaxial stress and reflection coefficients. Geophys. J. Int. 179 (3), 1584–1592. https://doi.org/10.1111/j.1365-246X.2009.04353.x.

Ma, X.Y., Wang, S.X., Zhao, J.G., et al., 2018. Velocity dispersion and fluid substitution in sandstone under partially saturated conditions. Appl. Geophys. 15 (2), 188–196. https://doi.org/10.1007/s11770-018-0683-8.

Marquardt, D.W., 1963. An algorithm for least-squares estimation of nonlinear parameters. J. Soc. Ind. Appl. Math. 11 (2), 431–441. https://doi.org/10.1137/0111030.

Mews, K.S., Lozovyi, S., 2025. Seismic and ultrasonic frequency measurements on partially saturated rocks under X-ray. Geophys. J. Int. 240 (3), 1705–1731. https://doi.org/10.1093/gji/ggaf017.

Pao, Y.H., 1984. Acoustoelasticity and ultrasonic measurement of residual stress. Phys. Acoust. 61–143. https://www.mendeley.com/catalogue.

Pei, X., Liu, Y., Lin, Z., et al., 2024. Anisotropic dynamic permeability model for porous media. Petrol. Explor. Dev. 51 (1), 193–202. https://doi.org/10.1016/S1876-3804(24)60016-9.

Pride, S.R., Berryman, J.G., Harris, J.M., 2004. Seismic attenuation due to wave-induced flow. J. Geophys. Res. Solid Earth 109 (B1), B01201. https://doi.org/10.1029/2003JB002639.

Qi, Q., Cao, J.X., Wang, X.J., et al., 2021. Influence of interface condition on reflection of elastic waves in fluid-saturated porous media. Geophysics 86 (4), MR223–MR233. https://doi.org/10.1190/geo2020-0624.1.

Shapiro, S.A., 2003. Elastic piezosensitivity of porous and fractured rocks. Geophysics 68 (2), 482–486. https://doi.org/10.1190/1.1567215.

Sharma, M.D., 2004. 3-D wave propagation in a general anisotropic poroelastic medium: reflection and refraction at an interface with fluid. Geophys. J. Int. 157 (2), 947–958. https://doi.org/10.1111/j.1365-246X.2004.02226.x.

Sharma, M.D., 2013. Effect of local fluid flow on reflection of plane elastic waves at the boundary of a double-porosity medium. Adv. Water Resour. 61, 62–73. https://doi.org/10.1016/j.advwatres.2013.09.001.

Shi, Z., He, X., Chen, D., et al., 2024. Seismic wave dispersion and attenuation resulting from multiscale wave-induced fluid flow in partially saturated porous media. Geophys. J. Int. 236 (2), 1172–1182. https://doi.org/10.1093/gji/ggad475.

Sripanich, Y., Vasconcelos, I., Tromp, J., et al., 2021. Stress-dependent elasticity and wave propagation—New insights and connections. Geophysics 86 (4), W47–W64. https://doi.org/10.1190/geo2020-0252.1.

Stoll, R.D., 1977. Acoustic waves in ocean sediments. Geophysics 42 (4), 715–725. https://doi.org/10.1190/1.1440741.

Sun, C., Fortin, J., Borgomano, J.V., et al., 2022. Influence of fluid distribution on seismic dispersion and attenuation in partially saturated limestone. J. Geophys. Res. Solid Earth 127 (5), e2021JB023867. https://doi.org/10.1029/2021JB023867.

Sun, W., Ba, J., Carcione, J.M., 2016. Theory of wave propagation in partially saturated double-porosity rocks: A triple-layer patchy model. Geophys. J. Int. 205 (1), 22–37. https://doi.org/10.1093/gji/ggv551.

Tang, X., 2011. A unified theory for elastic wave propagation through porous media containing cracks—An extension of Biot's poroelastic wave theory. Sci. China Earth Sci. 54, 1441–1452. https://doi.org/10.1007/s11430-011-4245-7.

Tang, X., Chen, X., Xu, X., 2012. A cracked porous medium elastic wave theory and its application to interpreting acoustic data from tight formations. Geophysics 77 (6), D245–D252. https://doi.org/10.1190/geo2012-0091.1.

Thurston, R.N., Brugger, K., 1964. Third-order elastic constants and the velocity of small amplitude elastic waves in homogeneously stressed media. Phys. Rev. 133 (6A), A1604. https://doi.org/10.1103/PhysRev.133.A1604.

Wang, E., Carcione, J.M., Ba, J., et al., 2020. Reflection and transmission of plane elastic waves at an interface between two double-porosity media: effect of local fluid flow. Surv. Geophys. 41, 283–322. https://doi.org/10.1007/s10712-019-09572-6.

Wang, E., Carcione, J.M., Cavallini, F., et al., 2021. Generalized thermo-poroelasticity equations and wave simulation. Surv. Geophys. 42, 133–157. https://doi.org/10.1007/s10712-020-09619-z.

Wang, Y.R., Zong, Z.Y., Yin, X.Y., 2022. Fluid discrimination incorporating amplitude variation with angle inversion and squirt flow of the fluid. Pet. Sci. 19 (4), 1592–1604. https://doi.org/10.1016/j.petsci.2022.03.007.

White, J.E., 1975. Computed seismic speeds and attenuation in rocks with partial gas saturation. Geophysics 40 (2), 224–232. https://doi.org/10.1190/1.1440520.

Winkler, K.W., McGowan, L., 2004. Nonlinear acoustoelastic constants of dry and saturated rocks. J. Geophys. Res. Solid Earth 109 (B10), B10204. https://doi.org/10.1029/2004JB003262.

Wu, K., Xue, Q., Adler, L., 1990. Reflection and transmission of elastic waves from a fluid-saturated porous solid boundary. J. Acoust. Soc. Am. 87 (6), 2349–2358. https://doi.org/10.1121/1.399081.

Yang, H., Fu, L.Y., 2025. Stress-dependent reflection and transmission of elastic waves in rocks with elastic-inelastic deformations under confining, uniaxial, and pure shear prestresses. IEEE Trans. Geosci. Rem. Sens. 63, 5910619. https://doi.org/10.1109/TGRS.2025.3558412.

Yang, J., Fu, L.Y., Han, T., et al., 2025. Thermoacoustoelasticity for elastic wave propagation in preheated and prestressed solid rocks. Rock Mech. Rock Eng. 58, 5143–5165. https://doi.org/10.1007/s00603-024-04361-z.

Zhang, H.X., He, B.S., 2015. Propagation and attenuation of P-waves in patchy saturated porous media. Appl. Geophys. 12 (3), 401–408. https://doi.org/10.1007/s11770-015-0497-x.

Zhao, L., Han, D.H., Yao, Q., et al., 2015. Seismic reflection dispersion due to wave-induced fluid flow in heterogeneous reservoir rocks. Geophysics 80 (3), D221–D235. https://doi.org/10.1190/geo2014-0307.1.

Zhao, Z., Yin, X., Zong, Z., 2019. Attenuation and dispersion characteristics of P wave in partially-saturated media with transverse squirt flow. Geophys. Prospect. Pet. 58 (1), 17–26. https://doi.org/10.3969/j.issn.1000-1441.2019.01.003 (in Chinese).

Zheng, P., Ding, B., Sun, X., 2017. Elastic wave attenuation and dispersion induced by mesoscopic flow in double-porosity rocks. Int. J. Rock Mech. Min. 91, 104–111. https://doi.org/10.1016/j.ijrmms.2016.11.018.

Zimmerman, R.W., Somerton, W.H., King, M.S., 1986. Compressibility of porous rocks. J. Geophys. Res. 91 (B12), 12765–12777. https://doi.org/10.1029/JB091iB12p12765.

Zong, Z., Chen, F., Yin, X., et al., 2023. Effect of stress on wave propagation in fluid-saturated porous thermoelastic media. Surv. Geophys. 44 (2), 425–462. https://doi.org/10.1007/s10712-022-09743-y.

Zong, Z.Y., Feng, Y.W., Chen, F.B., et al., 2025. Effects of multi-scale wave-induced fluid flow on seismic dispersion, attenuation and frequency-dependent anisotropy in periodic-layered porous-cracked media. Pet. Sci. 22 (2), 684–696. https://doi.org/10.1016/j.petsci.2024.11.006.